Search for Single Top Quark Production in 1.8-TeV Proton-Antiproton Collisions

Toshiaki KIKUCHI

A dissertation submitted to the Doctoral Program
in Physics in University of Tsukuba
in partial fulfillment of the requirements for the
degree of Doctor of philosophy (Science)

December, 1999

Abstract

We present a search for the single top quark production in the W-gluon fusion channel and the s-channel W^* channel in proton-antiproton collisions at $\sqrt{s} = 1.8$ TeV. The integrated luminosity of the data is 106 $\pm$ 4.1 pb^{-1}. We extract the number of signal events to be $1.3^{+4.2}_{-1.3}$ and the upper limit on the cross section of 13.5 pb at 95 % confidence level for single top quark production through the W-gluon fusion process. For single top quark production through s-channel W^* process, the estimated number of signal events is $6.4^{+7.3}_{-6.4}$ and the upper limit on the cross section is 12.9 pb at 95 % confidence level. For combined single top production search via the s-channel W^* and W-gluon fusion processes, we measure the cross section to be $5.2^{+4.9}_{-3.4}$(stat)$\pm$1.4(syst) pb and upper limit on the cross section of 18.6 pb at 95 % confidence level.

Acknowledgments

I would like to thank my supervisor, Professor Shin-hong Kim for his supports and insightful suggestions and continuous encouragements throughout my graduate career. I would like to thank Professor Koji Takikawa, the representative of the Japanese CDF collaboration, for educational advises and helpful suggestions. I would like to express my appreciation to Professor Luc Demortieir for his greatest supports, indispensable guidances to this study and the corrections of the notes of his kindness. I owe thank to the members of CDF top group for helpful comments and suggestions.

I wish to thank Drs. Kazuhiko Hara, Yoshihiro Seiya and Makoto Shimojima for their advises and comments. I am grateful to all members in High Energy Physics Laboratory at University of Tsukuba for their helpful supports and discussions. Especially, I would like to thank Drs. Hiroyuki Minato and Hirofumi Ikeda.

I would like to thank Ms. Carol Picciolo, Ms. Kyoko Kunori, Ms. Kazuko Kumashiro and Ms. Mutumi Uenishi for their constant support with their secretarial works.

Finally, I wish to thank my parents for their helps and supports.

This work was supported by the Ministry of Education, Science and Culture of Japan; the U.S. Department of Energy and National Science Foundation; the Italian Istituto Nazionale di Fisica Nucleare; the Natural Sciences and Engineering Research Council of Canada; the National Science Council of the Republic of China; and the A.P. Sloan Foundation.

The CDF collaboration

F. Abe,[17] H. Akimoto,[39] A. Akopian,[31] M. G. Albrow,[7] A. Amadon,[5] S. R. Amendolia,[27] D. Amidei,[20] J. Antos,[33] S. Aota,[37] G. Apollinari,[31] T. Arisawa,[39] T. Asakawa,[37] W. Ashmanskas,[5] M. Atac,[7] P. Azzi-Bacchetta,[25] N. Bacchetta,[25] S. Bagdasarov,[31] M. W. Bailey,[22] P. de Barbaro,[30] A. Barbaro-Galtieri,[18] V. E. Barnes,[29] B. A. Barnett,[15] M. Barone,[9] G. Bauer,[19] T. Baumann,[11] F. Bedeschi,[27] S. Behrends,[3] S. Belforte,[27] G. Bellettini,[27] J. Bellinger,[40] D. Benjamin,[35] J. Bensinger,[3] A. Beretvas,[7] J. P. Berge,[7] J. Berryhill,[5] S. Bertolucci,[9] S. Bettelli,[27] B. Bevensee,[26] A. Bhatti,[31] K. Biery,[7] C. Bigongiari,[27] M. Binkley,[7] D. Bisello,[25] R. E. Blair,[1] C. Blocker,[3] K. Bloom,[20] S. Blusk,[30] A. Bodek,[30] W. Bokhari,[26] G. Bolla,[29] Y. Bonushkin,[4] D. Bortoletto,[29] J. Boudreau,[28] L. Breccia,[2] C. Bromberg,[21] N. Bruner,[22] R. Brunetti,[2] E. Buckley-Geer,[7] H. S. Budd,[30] K. Burkett,[11] G. Busetto,[25] A. Byon-Wagner,[7] K. L. Byrum,[1] M. Campbell,[20] A. Caner,[27] W. Carithers,[18] D. Carlsmith,[40] J. Cassada,[30] A. Castro,[25] D. Cauz,[36] A. Cerri,[27] P. S. Chang,[33] P. T. Chang,[33] H. Y. Chao,[33] J. Chapman,[20] M. -T. Cheng,[33] M. Chertok,[34] G. Chiarelli,[27] C. N. Chiou,[33] F. Chlebana,[7] L. Christofek,[13] R. Cropp,[14] M. L. Chu,[33] S. Cihangir,[7] A. G. Clark,[10] M. Cobal,[27] E. Cocca,[27] M. Contreras,[5] J. Conway,[32] J. Cooper,[7] M. Cordelli,[9] D. Costanzo,[27] C. Couyoumtzelis,[10] D. Cronin-Hennessy,[6] R. Culbertson,[5] D. Dagenhart,[38] T. Daniels,[19] F. DeJongh,[7] S. Dell'Agnello,[9] M. Dell'Orso,[27] R. Demina,[7] L. Demortier,[31] M. Deninno,[2] P. F. Derwent,[7] T. Devlin,[32] J. R. Dittmann,[6]

S. Donati,[27] J. Done,[34] T. Dorigo,[25] N. Eddy,[13] K. Einsweiler,[18]
J. E. Elias,[7] R. Ely,[18] E. Engels, Jr.,[28] W. Erdmann,[7] D. Errede,[13]
S. Errede,[13] Q. Fan,[30] R. G. Feild,[41] Z. Feng,[15] C. Ferretti,[27] I. Fiori,[2]
B. Flaugher,[7] G. W. Foster,[7] M. Franklin,[11] J. Freeman,[7] J. Friedman,[19]
H. Frisch,[5] Y. Fukui,[17] S. Gadomski,[14] S. Galeotti,[27] M. Gallinaro,[26]
O. Ganel,[35] M. Garcia-Sciveres,[18] A. F. Garfinkel,[29] C. Gay,[41] S. Geer,[7]
D. W. Gerdes,[20] P. Giannetti,[27] N. Giokaris,[31] P. Giromini,[9] G. Giusti,[27]
M. Gold,[22] A. Gordon,[11] A. T. Goshaw,[6] Y. Gotra,[28] K. Goulianos,[31]
H. Grassmann,[36] C. Green,[29] L. Groer,[32] C. Grosso-Pilcher,[5]
G. Guillian,[20] J. Guimaraes da Costa,[15] R. S. Guo,[33] C. Haber,[18]
E. Hafen,[19] S. R. Hahn,[7] R. Hamilton,[11] T. Handa,[12] R. Handler,[40]
W. Hao,[35] F. Happacher,[9] K. Hara,[37] A. D. Hardman,[29] R. M. Harris,[7]
F. Hartmann,[16] J. Hauser,[4] E. Hayashi,[37] J. Heinrich,[26] A. Heiss,[16]
B. Hinrichsen,[14] K. D. Hoffman,[29] C. Holck,[26] R. Hollebeek,[26]
L. Holloway,[13] Z. Huang,[20] B. T. Huffman,[28] R. Hughes,[23] J. Huston,[21]
J. Huth,[11] H. Ikeda,[37] M. Incagli,[27] J. Incandela,[7] G. Introzzi,[27]
J. Iwai,[39] Y. Iwata,[12] E. James,[20] H. Jensen,[7] U. Joshi,[7] E. Kajfasz,[25]
H. Kambara,[10] T. Kamon,[34] T. Kaneko,[37] K. Karr,[38] H. Kasha,[41]
Y. Kato,[24] T. A. Keaffaber,[29] K. Kelley,[19] R. D. Kennedy,[7]
R. Kephart,[7] D. Kestenbaum,[11] D. Khazins,[6] T. Kikuchi,[37] M. Kirk,[3]
B. J. Kim,[27] H. S. Kim,[14] S. H. Kim,[37] Y. K. Kim,[18] L. Kirsch,[3]
S. Klimenko,[8] D. Knoblauch,[16] P. Koehn,[23] A. Köngeter,[16] K. Kondo,[37]
J. Konigsberg,[8] K. Kordas,[14] A. Korytov,[8] E. Kovacs,[1] W. Kowald,[6]
J. Kroll,[26] M. Kruse,[30] S. E. Kuhlmann,[1] E. Kuns,[32] K. Kurino,[12]
T. Kuwabara,[37] A. T. Laasanen,[29] S. Lami,[27] S. Lammel,[7]
J. I. Lamoureux,[3] M. Lancaster,[18] M. Lanzoni,[27] G. Latino,[27]

T. LeCompte,[1] S. Leone,[27] J. D. Lewis,[7] M. Lindgren,[4] T. M. Liss,[13]
J. B. Liu,[30] Y. C. Liu,[33] N. Lockyer,[26] O. Long,[26] M. Loreti,[25]
D. Lucchesi,[27] P. Lukens,[7] S. Lusin,[40] J. Lys,[18] K. Maeshima,[7]
P. Maksimovic,[11] M. Mangano,[27] M. Mariotti,[25] J. P. Marriner,[7]
G. Martignon,[25] A. Martin,[41] J. A. J. Matthews,[22] P. Mazzanti,[2]
K. McFarland,[30] P. McIntyre,[34] P. Melese,[31] M. Menguzzato,[25]
A. Menzione,[27] E. Meschi,[27] S. Metzler,[26] C. Miao,[20] T. Miao,[7]
G. Michail,[11] R. Miller,[21] H. Minato,[37] S. Miscetti,[9] M. Mishina,[17]
S. Miyashita,[37] N. Moggi,[27] E. Moore,[22] Y. Morita,[17] A. Mukherjee,[7]
T. Muller,[16] A. Munar,[27] P. Murat,[27] S. Murgia,[21] M. Musy,[36]
H. Nakada,[37] T. Nakaya,[5] I. Nakano,[12] C. Nelson,[7] D. Neuberger,[16]
C. Newman-Holmes,[7] C.-Y. P. Ngan,[19] H. Niu,[3] L. Nodulman,[1]
A. Nomerotski,[8] S. H. Oh,[6] T. Ohmoto,[12] T. Ohsugi,[12] R. Oishi,[37]
M. Okabe,[37] T. Okusawa,[24] J. Olsen,[40] C. Pagliarone,[27] R. Paoletti,[27]
V. Papadimitriou,[35] S. P. Pappas,[41] N. Parashar,[27] A. Parri,[9]
D. Partos,[3] J. Patrick,[7] G. Pauletta,[36] M. Paulini,[18] A. Perazzo,[27]
L. Pescara,[25] M. D. Peters,[18] T. J. Phillips,[6] G. Piacentino,[27]
M. Pillai,[30] K. T. Pitts,[7] R. Plunkett,[7] A. Pompos,[29] L. Pondrom,[40]
J. Proudfoot,[1] F. Ptohos,[11] G. Punzi,[27] K. Ragan,[14] D. Reher,[18]
M. Reischl,[16] A. Ribon,[25] F. Rimondi,[2] L. Ristori,[27] W. J. Robertson,[6]
A. Robinson,[14] T. Rodrigo,[27] S. Rolli,[38] L. Rosenson,[19] R. Roser,[13]
T. Saab,[14] W. K. Sakumoto,[30] D. Saltzberg,[4] A. Sansoni,[9] L. Santi,[36]
H. Sato,[37] P. Schlabach,[7] E. E. Schmidt,[7] M. P. Schmidt,[41] A. Scott,[4]
A. Scribano,[27] S. Segler,[7] S. Seidel,[22] Y. Seiya,[37] F. Semeria,[2] T. Shah,[19]
M. D. Shapiro,[18] N. M. Shaw,[29] P. F. Shepard,[28] T. Shibayama,[37]
M. Shimojima,[37] M. Shochet,[5] J. Siegrist,[18] A. Sill,[35] P. Sinervo,[14]

P. Singh,[13] K. Sliwa,[38] C. Smith,[15] F. D. Snider,[15] J. Spalding,[7]
T. Speer,[10] P. Sphicas,[19] F. Spinella,[27] M. Spiropulu,[11] L. Spiegel,[7]
L. Stanco,[25] J. Steele,[40] A. Stefanini,[27] R. Ströhmer,[7a] J. Strologas,[13]
F. Strumia, [10] D. Stuart,[7] K. Sumorok,[19] J. Suzuki,[37] T. Suzuki,[37]
T. Takahashi,[24] T. Takano,[24] R. Takashima,[12] K. Takikawa,[37]
M. Tanaka,[37] B. Tannenbaum,[4] F. Tartarelli,[27] W. Taylor,[14]
M. Tecchio,[20] P. K. Teng,[33] Y. Teramoto,[24] K. Terashi,[37] S. Tether,[19]
D. Theriot,[7] T. L. Thomas,[22] R. Thurman-Keup,[1] M. Timko,[38]
P. Tipton,[30] A. Titov,[31] S. Tkaczyk,[7] D. Toback,[5] K. Tollefson,[30]
A. Tollestrup,[7] H. Toyoda,[24] W. Trischuk,[14] J. F. de Troconiz,[11]
S. Truitt,[20] J. Tseng,[19] N. Turini,[27] T. Uchida,[37] F. Ukegawa,[26]
J. Valls,[32] S. C. van den Brink,[15] S. Vejcik, III,[20] G. Velev,[27]
I. Volobouev,[18] R. Vidal,[7] R. Vilar,[7a] D. Vucinic,[19] R. G. Wagner,[1]
R. L. Wagner,[7] J. Wahl,[5] N. B. Wallace,[27] A. M. Walsh,[32] C. Wang,[6]
C. H. Wang,[33] M. J. Wang,[33] A. Warburton,[14] T. Watanabe,[37]
T. Watts,[32] R. Webb,[34] C. Wei,[6] H. Wenzel,[16] W. C. Wester, III,[7]
A. B. Wicklund,[1] E. Wicklund,[7] R. Wilkinson,[26] H. H. Williams,[26]
P. Wilson,[7] B. L. Winer,[23] D. Winn,[20] D. Wolinski,[20] J. Wolinski,[21]
S. Worm,[22] X. Wu,[10] J. Wyss,[27] A. Yagil,[7] W. Yao,[18] K. Yasuoka,[37]
G. P. Yeh,[7] P. Yeh,[33] J. Yoh,[7] C. Yosef,[21] T. Yoshida,[24] I. Yu,[7]
A. Zanetti,[36] F. Zetti,[27] and S. Zucchelli[2]

(CDF Collaboration)

[1] *Argonne National Laboratory, Argonne, Illinois 60439*

[2] *Istituto Nazionale di Fisica Nucleare, University of Bologna, I-40127 Bologna, Italy*

[3] *Brandeis University, Waltham, Massachusetts 02254*

[4] *University of California at Los Angeles, Los Angeles, California 90024*

[5] *University of Chicago, Chicago, Illinois 60637*

[6] *Duke University, Durham, North Carolina 27708*

[7] *Fermi National Accelerator Laboratory, Batavia, Illinois 60510*

[8] *University of Florida, Gainesville, Florida 32611*

[9] *Laboratori Nazionali di Frascati, Istituto Nazionale di Fisica Nucleare, I-00044 Frascati, Italy*

[10] *University of Geneva, CH-1211 Geneva 4, Switzerland*

[11] *Harvard University, Cambridge, Massachusetts 02138*

[12] *Hiroshima University, Higashi-Hiroshima 724, Japan*

[13] *University of Illinois, Urbana, Illinois 61801*

[14] *Institute of Particle Physics, McGill University, Montreal H3A 2T8, and University of Toronto,*

Toronto M5S 1A7, Canada

[15] *The Johns Hopkins University, Baltimore, Maryland 21218*

[16] *Institut für Experimentelle Kernphysik, Universität Karlsruhe, 76128 Karlsruhe, Germany*

[17] *National Laboratory for High Energy Physics (KEK), Tsukuba, Ibaraki 305, Japan*

[18] *Ernest Orlando Lawrence Berkeley National Laboratory, Berkeley, California 94720*

[19] *Massachusetts Institute of Technology, Cambridge, Massachusetts 02139*

[20] *University of Michigan, Ann Arbor, Michigan 48109*

[21] *Michigan State University, East Lansing, Michigan 48824*

[22] *University of New Mexico, Albuquerque, New Mexico 87131*

[23] *The Ohio State University, Columbus, Ohio 43210*

[24] *Osaka City University, Osaka 588, Japan*

[25] *Universita di Padova, Istituto Nazionale di Fisica Nucleare, Sezione di Padova, I-35131 Padova, Italy*

[26] *University of Pennsylvania, Philadelphia, Pennsylvania 19104*

[27] *Istituto Nazionale di Fisica Nucleare, University and Scuola Normale Superiore of Pisa, I-56100 Pisa, Italy*

[28] *University of Pittsburgh, Pittsburgh, Pennsylvania 15260*

[29] *Purdue University, West Lafayette, Indiana 47907*

[30] *University of Rochester, Rochester, New York 14627*

[31] *Rockefeller University, New York, New York 10021*

[32] *Rutgers University, Piscataway, New Jersey 08855*

[33] *Academia Sinica, Taipei, Taiwan 11530, Republic of China*

[34] *Texas A&M University, College Station, Texas 77843*

[35] *Texas Tech University, Lubbock, Texas 79409*

[36] *Istituto Nazionale di Fisica Nucleare, University of Trieste/ Udine, Italy*

[37] *University of Tsukuba, Tsukuba, Ibaraki 305, Japan*

[38] *Tufts University, Medford, Massachusetts 02155*

[39] *Waseda University, Tokyo 169, Japan*

[40] *University of Wisconsin, Madison, Wisconsin 53706*

[41] *Yale University, New Haven, Connecticut 06520*

Contents

1 Introduction **19**

1.1 The observation of the top quark 19

1.2 Single top quark production 21

2 The experimental apparatus **26**

2.1 Tevatron collider 26

2.2 The CDF detector 27

2.2.1 Coordinate system 28

2.2.2 Tracking system 28

2.2.3 Calorimetry 31

2.2.4 Muon system 33

2.2.5 Triggers 34

3 Event selection **44**

3.1 High P_T electron selection 45

3.2 High P_T muon selection 46

3.3 Missing transverse energy ($\not\!\!E_T$) 48

3.4 Z boson production and dilepton events removal 49

3.5 Jet identification 50

3.6 B-tagging 51
3.6.1 SVX b-tagging algorithm 52
3.6.2 SLT b-tagging algorithm 52
3.7 Monte Carlo simulations 53
3.8 Signal acceptance for W+2 jet events 53
3.9 Expected background and observed data 55

4 Search for single top quark production through the W-gluon fusion process 60
4.1 Reconstructed top mass window cut 61
4.2 Likelihood fit of $\boldsymbol{Q \times \eta}$ distribution 63
4.3 Systematic uncertainty 64
4.3.1 Systematic uncertainty on the shape 65
4.3.2 Systematic uncertainty on the acceptance 68
4.4 Cross section limit 70

5 Search for single top quark production through the s-channel W^* process 81
5.1 Top mass reconstruction 81
5.2 Cross section limit from predicted and observed event rates 82
5.3 Likelihood fit of the reconstructed mass distribution . . . 84
5.3.1 Binned likelihood fit 84
5.3.2 Unbinned likelihood fit 85
5.4 Systematic uncertainty 88
5.4.1 Systematic uncertainty on the shape of the reconstructed mass distribution 88
5.4.2 Systematic uncertainty on the acceptance 91

5.5 Cross section limit 91
5.6 Checks of the likelihood method 92
5.6.1 Check of the likelihood fit 93
5.6.2 Check of the upper limit calculations 94

6 Upper limit on the combined cross section of single top quark production via the s-channel W^* and W-gluon fusion processes 104
6.1 Likelihood fit 105
6.2 Cross section limit 107
6.3 Systematic uncertainty 108
6.3.1 The shapes of $Q \times \eta$ distribution and top mass distribution 108
6.3.2 The acceptance of event selection 111

7 Conclusion 122

List of Figures

1.1 $t\bar{t}$ production processes. $q\bar{q} \to t\bar{t}$ and $gg \to t\bar{t}$. 24

1.2 Diagrams for single top quark production processes . . . 25

2.1 Diagram of the Tevatron accelerator complex 36

2.2 CDF coordinate system 37

2.3 Perspective view of the CDF detector 38

2.4 Cross-sectional view of a quadrant of the CDF detector . 39

2.5 Schematic view of one barrel of the SVX detector 40

2.6 Transverse view at the endplate of the CTC showing the wire cells 41

2.7 Perspective view of a central calorimeter wedge 42

2.8 The coverage of muon chambers 43

3.1 Jet multiplicity distribution with uncorrected $E_T > 15$ GeV and$|\eta| < 2.0$. 58

3.2 Cross section view of an event containing a secondary vertex 59

4.1 P_T distribution for the W-gluon fusion single top events with HERWIG Monte Carlo. 72

4.2 Reconstructed top mass distributions for data (a), single top events through the W-gluon fusion process (b), single top events through the s-channel W^* channel (c), VECBOS $Wb\bar{b}$ (d), HERWIG $t\bar{t}$ (e) and PYTHIA Wc (f). . . 73
4.3 Reconstructed top mass distributions for PYTHIA WW (a), PYTHIA WZ (b), VECBOS Zbb (c). 74
4.4 Reconstructed top mass distributions for single top events through the W-gluon fusion process (a) and single top events through the s-channel W^* process (b). Hatched histograms show the events with the right b-jet assignment. 75
4.5 Diagrams for single top quark production through W-gluon fusion processes with top (not $\bar{t}$) quark. 76
4.6 Q$\times\eta$ distributions for data (a), single top events through the W-gluon fusion process (b), single top events through the s-channel W^* process (c), VECBOS $Wb\bar{b}$ (d), HERWIG $t\bar{t}$ (e) and PYTHIA Wc (f). 77
4.7 Fitted Q$\times\eta$ distribution. The points show the CDF data, the dashed histogram shows the fitted background, and the solid histogram shows the fitted signal plus background. 78

4.8 Q×η distributions for the standard HERWIG signal events with MRSD_' parton distribution (a), PYTHIA Monte Carlo signal events with systematic shift (b), PYTHIA without initial state radiation (c), PYTHIA without initial state radiation and with parton -jet matching (d), and HERWIG signal events with CTEQ4L parton distribution (e). 79

4.9 Smeared likelihood $L'(\sigma)$ as a function of the cross section of single top production through the W-gluon fusion process for the CDF data. 80

5.1 Reconstructed top mass distributions for data (a), single top through the W-gluon fusion process (b), single top through the W^* process (c), VECBOS $Wb\bar{b}$ (d), HERWIG $t\bar{t}$ (e), and PYTHIA Wc (f). 95

5.2 Reconstructed top mass distributions for PYTHIA WW (a), PYTHIA WZ (b), and VECBOS Zbb (c). 96

5.3 Reconstructed top mass distributions for single top through the W-gluon fusion process (a) and single top through the W^* process (b). Hatched histograms show the events with the right b-jet assignment. 97

5.4 Reconstructed top mass distribution. The points show the data, the dashed histogram shows the fitted background, and the solid histogram shows fitted signal plus background. 98

5.5 Reconstructed top mass distributions for s-channel W^* signal events generated with standard PYTHIA Monte Carlo (a), PYTHIA with no initial state radiation (b), with no initial state and with parton -jet matching (c), HERWIG with parton distribution of CTEQ4L (d), with positively shifted jet energy (e) and with negatively shifted jet energy (f). 99

5.6 Jet multiplicity distribution with uncorrected $E_T > 15$ GeV and $|\eta| < 2.0$ for s-channel W^* signal Monte Carlo. The solid histogram is that for the default jet energy scale, the dotted histogram is for negatively shifted jet E_T, and the dashed histogram is for positively shifted jet E_T. . . 100

5.7 Smeared likelihood $L'(\sigma)$ as a function of the W^* single top cross section in the data. 101

5.8 Test of the likelihood fit with pseudo-experiments consisting of N_b background and N_s signal events, where N_b is a Poisson fluctuation of the number of events predicted in Table 5.1, and N_s is a Poisson fluctuation of the fit result on the data (6.6 events). The distribution of the fitted number of signal events (a) and the corresponding pulls distribution (b). 102

5.9 Distribution of the fitted number of signal events for pseudo-experiment samples. Each sample consists of N_b background and N_s signal events, where N_b is a Poisson fluctuation of the number of events predicted in Table 5.1, and N_s is a Poisson fluctuation of the unsmeared upper limit on the signal. The fitted number of signal events is equal to or less than 6.6 events in 3.5% of the pseudo-experiments. 103

6.1 Reconstructed top mass distributions for data (a), single top in the W-gluon fusion channel (b), single top in the $W^\star$ channel (c), VECBOS $Wb\bar{b}$ (d), and HERWIG $t\bar{t}$ (e), after selection of double b-tagged events. 118

6.2 Fitted Q×η distribution. The points show the data, the dashed histogram shows the fitted background, and the solid histogram shows the fitted signal plus background. . 119

6.3 Fitted reconstructed top mass distribution for double b-tagged W+2 jet events. The points show the data, the dashed histogram shows the fitted background, and the solid histogram shows fitted signal plus background. . . . 120

6.4 The likelihood $L(\sigma_{Wg}, \sigma_{W^*})$ 121

List of Tables

1.1 Three generations of leptons and quarks 20

1.2 The uncertainty on the theoretical cross section 22

2.1 Summary of CDF calorimeter properties. E_T is the transverse energy and E is the energy given in GeV. 31

3.1 Electron selection 47

3.2 Muon selection criteria 48

3.3 $Z \to ee$ second leg selection 49

3.4 $Z \to \mu\mu$ second leg selection 49

3.5 The expected numbers of events for single-top production through the s-channel W^* and W-gluon fusion processes. 54

3.6 Expected and observed numbers of SVX b-tagged W+2jet events. 57

4.1 Expected number of events and $S/\sqrt{B}$ for several top mass window cuts. The QCD background includes all backgrounds except for the $t\bar{t}$ background. 62

4.2 Parameter input and output values for the fit of the Q$\times\eta$ distribution with background constraints. 65

4.3 Parameter input and output values for the fit of the Q×η distribution without background constraints. 65
4.4 Systematic uncertainties affecting the shape of the $Q \times \eta$ distribution. 68
4.5 Systematic uncertainties affecting the acceptance. 69
4.6 The absolute uncertainty on the shape Δ_i and the relative uncertainty on the acceptance δ_i 71

5.1 Parameter input and output values for the binned likelihood fit of the reconstructed top mass distribution with background constraints. 85
5.2 Parameter output values for the binned likelihood fit of the reconstructed top mass distribution without background constraints, but forcing the parameters to be positive. . . 86
5.3 Parameter output values for the binned likelihood fit of the reconstructed top mass distribution without background constraints and without forcing the parameters to be positive. 86
5.4 Parameter input and output values for the unbinned likelihood fit with background constraints. 87
5.5 Parameter output values for the unbinned likelihood fit without background constraints. 87
5.6 Systematic uncertainties affecting the shape of the reconstructed top mass distribution. 90
5.7 Systematic uncertainties affecting the acceptance. 91
5.8 The absolute uncertainty on the shape Δ_i and the relative uncertainty on the acceptance δ_i 93

6.1 Fit parameter input and output values for the binned likelihood fit. 107
6.2 Shift on the cross section limit due to the shape uncertainty 110
6.3 Input of the uncertainty affecting the acceptance in the likelihood L_1 for the single b-tagged events. 115
6.4 Input of the uncertainty affecting the acceptance in the likelihood L_2 for the double b-tagged events. 115
6.5 Shift on the cross section limit due to the acceptance . . 116
6.6 Shift on the cross section 117

Chapter 1

Introduction

The Standard Model has been successful in explaining and predicting the experimental results of high energy physics. It consists of quantum chromodynamics (QCD) for the strong interaction and electroweak theory which is the unified theory of the electromagnetic interaction and the weak interaction. Each interaction between quarks and leptons is mediated by bosons: gluons for strong interaction, photons for electromagnetic interaction and W and Z bosons for weak interaction. There are leptons and quarks of six types with three generations as shown in Table 1. The top quark makes a weak isospin doublet of the third generation with the bottom quark.

1.1 The observation of the top quark

Due to the inferences based on experimental results and theoretical reasons, the existence of the top quark is predicted and its discovery is awaited for a long time since the observation of bottom quark. The target

$$\begin{pmatrix} u \\ d \end{pmatrix} \begin{pmatrix} c \\ s \end{pmatrix} \begin{pmatrix} t \\ b \end{pmatrix}$$

$$\begin{pmatrix} e \\ \nu_e \end{pmatrix} \begin{pmatrix} \mu \\ \nu_\mu \end{pmatrix} \begin{pmatrix} \tau \\ \nu_\tau \end{pmatrix}$$

Table 1.1: Three generations of leptons and quarks

mass range of the top quark search has been raised as the experiments have set the new lower limit because the Standard Model does not predict any quark masses. At last the evidence of the top quark production was reported by the CDF collaboration[1] in 1994. In the next year the discovery of the top quark was established with more statistics of the data by both the CDF and DØ collaborations[2][3]. The primary productions of the top quark in 1.8 TeV proton-antiproton collisions are the $t\bar{t}$ pair productions through gluon-gluon fusion ($gg \rightarrow t\bar{t}$) and quark-antiquark annihilation ($q\bar{q} \rightarrow t\bar{t}$) shown in Figure 1.1. The latter process is the dominant one. As a top quark is very heavy, it decays to a W boson and a bottom quark before a meson is composed of the top quark. The final states are separated into the following three modes in accordance with the number of electrons or muons from W boson decay: Dilepton mode has $l\nu l\nu bb$ in the final state where l means an electron or a muon. Lepton+jets mode has $l\nu qqbb$ in the final state. Multijets mode has $qqqqbb$ in the final state. $t\bar{t}$ production was observed in all decay modes.

The combined top quark mass of CDF and DØ is extracted to be

174.1 ± 5.1 GeV/c^2 [4]. The measured cross section is 5.5 ± 1.8 pb in DØ and $6.5^{+1.7}_{-1.4}$ pb in CDF with acceptance calculations with the top quark mass of 173.3 GeV/c^2 and 175.0 GeV/c^2 respectively. These measurements are consistent with the predicted cross section of 5 pb by theory [5].

1.2 Single top quark production

Standard Model predicts the existence of single top quark production trough the following three processes: In W-gluon fusion process a top quark is generated with t-channel W exchange. In s-channel W^* process a pair of a top quark and an anti-bottom quark is produced through W^*. In tW production a pair of a top quark and a W boson is produced via $gb \to tW$. The diagrams for these three processes are shown in Figure 1.2.

The top quark is produced through a W-t-b coupling in the single top quark production. It is different from the $t\bar{t}$ production with strong coupling. So the observation of the single top quark production is meaningful for probing the charged current weak interaction of the top quark. Since the cross section of the single top quark production is proportional to a top quark partial width $\Gamma(t \to Wb)$, which is proportional to $|V_{tb}|^2$, the measurement of the cross section of the single top quark production yields $|V_{tb}|$ without assuming of the unitarity of the three generations in Cabibbo-Kobayashi-Maskawa matrix. For a top quark mass of 175 GeV/c^2, in 1.8-TeV $p\bar{p}$ collisions the predicted cross sections of the single top production are 1.7 ± 0.3 pb for W-gluon fusion process [6] and

Systematic sources	W^*	Wg
Scale variation	4%	10%
Parton distribution	4%	10%
Top quark mass ($\pm$ 5.1 GeV/c^2)	13%	9%
Total	14%	17%

Table 1.2: The uncertainty on the theoretical cross section

0.7 $\pm$ 0.1 pb for s-channel W^* process [7][8][9] with the calculation of next-to-leading order. uses the The uncertainty on the cross section is 17% for the W-gluon fusion process and 14% for the s-channel W^* process which will be incorporated to the measurement of $|V_{tb}|$. Table 1.2 lists the uncertainties on the theoretical cross sections. In the table the uncertainty due to the top quark mass uncertainty of 5.1 GeV/c^2 from experiments can be reduced by future measurements and the cross section of single top quark production through s-channel W^* process will have still smaller uncertainty than that through W-gluon fusion process. If the measured cross section could be significantly smaller than the Standard Model prediction, the $|V_{tb}|$ would be small and which indicate the existence of the fourth generation. If the measured cross section could have the excess from the prediction, it would suggest the existence of the non-Standard Model. As the single top quark production cross section through $gb \to tW$ process is about five times smaller than that through s-channel W^* process at Tevatron, it is not a good target to search now.

The final state of the W-gluon fusion processes is a top quark, a bottom quark and a light quark. Since the bottom quark from the gluon

splitting in this process is soft, the signal is detected as an event with a W boson, a b-jet and a light quark jet. The s-channel W^* signal has a W boson and two b-jets. So both processes have a W boson and two high P_T jets.

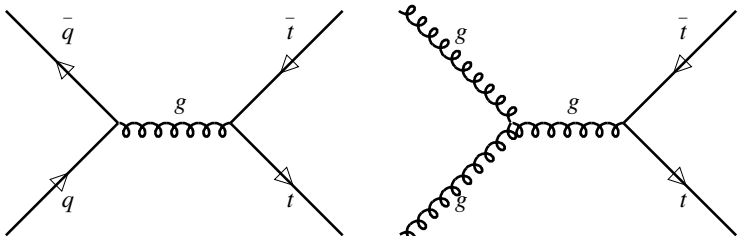

Figure 1.1: $t\bar{t}$ production processes. $q\bar{q} \to t\bar{t}$ and $gg \to t\bar{t}$.

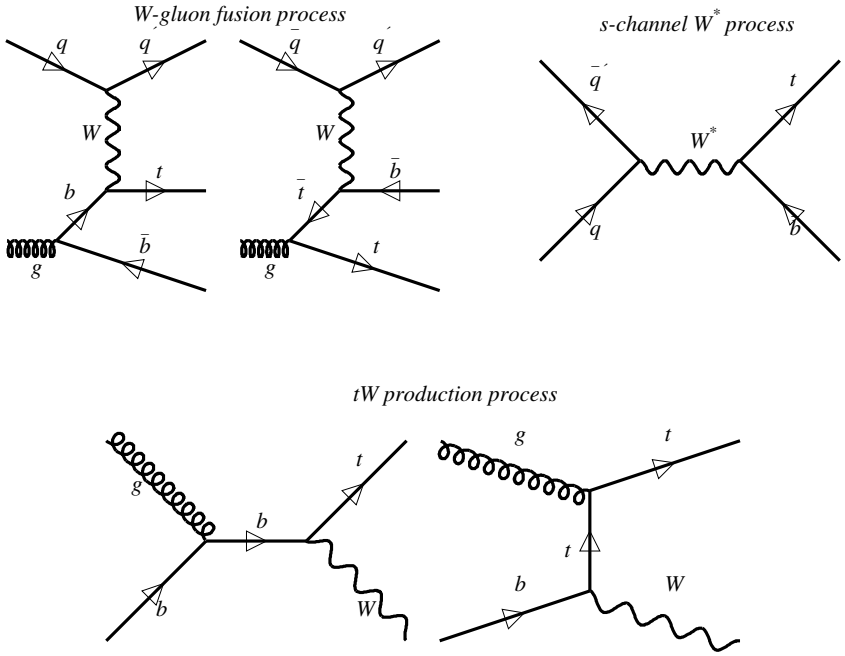

Figure 1.2: Diagrams for single top quark production processes

Chapter 2

The experimental apparatus

2.1 Tevatron collider

The Tevatron accelerator provide proton and antiproton colliding at a center of mass energy of 1.8 TeV. The Tevatron accelerator collider complex consists of five accelerators as shown in Figure 2.1. Particles are accelerated to higher energy at each accelerator. The Cockcroft-Walton accelerator makes negatively charged hydrogen ions and accelerates it to 750 KeV. The 500-feet long Linear accelerator accelerates the H^- ions from 750 KeV to 400 MeV. Then the ions pass through a carbon foil which removes the electrons, leaving only the protons. The proton energy is raised to 8 GeV by the Booster which is a synchrotron of 500 feet in diameter. And the next stage of the accelerator is the Main Ring which is a synchrotron of four mile in circumference. The Main Ring accelerates protons to 150 GeV. To produce antiprotons, protons are first accelerated to an energy of 120 GeV in Main Ring, extracted, transported to a target area, and focused on the target. The collisions in the target produce a

wide range of secondary particles including many antiprotons. These anti-protons are selected and transported to the Debuncher ring where they are reduced in size by stochastic cooling. And they are transferred to the Accumulator ring for storage. When a sufficient number has been produced, the antiprotons are reinjected into the Main Ring and passed down into the Tevatron ring where they are accelerated simultaneously with counterrotating beam of protons to an energy of 900 GeV. The bunches of protons and antiprotons cross with every 3.5 μs.

The luminosity is calculated by the equation:

$$L = \frac{N_p N_{\bar{p}} f B}{4\pi\epsilon\beta} \tag{2.1}$$

where N_p and $N_{\bar{p}}$ is the number of protons and antiprotons in a bunch respectively, f is a revolution frequency of the bunch, B is the number of bunches of each type, ϵ is an emittance, and β is a betatron oscillation length. The typical values of N_p and $N_{\bar{p}}$ are 1-2 $\times 10^{11}$ and 4-7 $\times 10^{10}$ respectively. The revolution frequency is about 50 kHz. The number of bunches is six. The emittance is 2.6 $\times 10^{-3}$ mm $\cdot$ mrad. The betatron oscillation length is 0.5 m. Typical luminosity is 0.5×10^{31} cm$^{-2}\cdot$sec^{-1} for RUN1A and 1.6×10^{31} cm$^{-2}\cdot$sec^{-1} for RUN1B.

2.2 The CDF detector

The CDF detector[10] is a general purpose detector designed to study the physics in $\bar{p}p$ collisions at the center of mass energy of 1.8 TeV. Figure 2.3 and Figure 2.4 show a perspective view and a cross-sectional view of the CDF detector respectively. The detector is separated into

roughly three categories: the tracking chambers, the calorimeters and the muon chambers. The chambers are placed in the three regions, central, end-plug and forward region and surrounding the collision point of particles.

2.2.1 Coordinate system

The coordinate system of CDF is defined as shown in Figure 2.2. Origin of the coordinate system is defined as the collision point of the CDF detector. Z direction is defined as the momentum direction of the proton, and x direction is defined as the radial direction of the Tevatron ring. Pseudo-rapidity η is used to show the angle: $\eta = -ln(\tan\frac{\theta}{2})$, which is an approximation of Lorentz invariant variable, rapidity $\frac{1}{2} \cdot ln(\frac{E+P_Z}{E-P_Z})$ at high energy $E \approx P$. Transverse energy and momentum are defined by $E_T = E\sin\theta$ and $P_T = P\sin\theta$, respectively.

2.2.2 Tracking system

The tracking system in the central region consists of three subsystems, a silicon vertex detector(SVX), a vertex drift chamber(VTX) and a central tracking drift chamber(CTC).

A superconducting solenoid covers the tracking system and generates a 1.4 T magnetic field along the incident beam direction. It allows precise momentum determination of charged particles in the central region.

Superconducting solenoid

The superconducting solenoid magnet coil is 4.8 m long and 1.5 m in radius. The coil is made of 1164 turns of an aluminum-stabilized NbTi/Cu superconductor. The steel magnet yoke is placed outside the central calorimeter to return the magnetic field flux.

Silicon vertex detector (SVX)

The silicon vertex detector(SVX) [13] [14][15] is a tracking detector closest to an interaction point with surrounding the 1.9 cm radius beam pipe. The SVX is designed to detect the secondary vertices from heavy flavor decay especially b hadrons of which the mean decay length is about 400 μm. The SVX consists of two barrels aligned end-to-end along the z axis. The schematic view of one barrel is shown in Figure 2.5. Each barrel is divided azimuthally into 12 wedges and radially into 4 concentric layers. Each layer contains 3 rectangular strip detectors with a size of 3 cm $\times$ 8.5 cm. The SVX has 46,080 channels which is about one third of all the channels for the whole CDF detector. The strip lines are running parallel to the beam line and provide the hit information in r-ϕ plane. The strip pitch is 60 μm for the inner three layers and 55 μm for the fourth layer. The SVX single hit resolution is measured to be 13 μm in r-ϕ plane. And the resolution of the impact parameter relative to the primary vertex is 17 μm.

The total coverage of SVX is 51 cm in z direction. As the spread of the $p\bar{p}$ collisions is 60 cm in a standard deviation, the SVX acceptance is 60 % in $p\bar{p}$ collisions. The SVX detector was used in RUN1A and replaced by the SVX' detector in RUN1B. The SVX' is very similar to

the SVX. The SVX' is an AC-coupled device for reducing noise though the SVX is a DC-coupled device. The SVX' is also improved to be more radiation-hard for the higher luminosity.

Vertex drift chamber (VTX)

The vertex drift chamber lies outside the SVX. The VTX consists of 28 modules of octagonal time projection chamber along the z axis. The inner 18 modules contain 16 sense wires perpendicular to the radial direction. The outer 10 modules contain 24 sense wires. It provides tracking information in r-z plane for each of the eight azimuthal sections within r $<$ 220 mm and $|\eta| < 3.3$. The VTX is primarily used to identify the z position of the primary vertex, that is, event vertex. The event vertex in z direction is determined with a resolution of about 1 mm.

Central tracking chamber (CTC)

The central tracking chamber(CTC) is a 1.3 m in a diameter and 3.2 m long cylindrical drift chamber with 84 layers of sense wires arranged into 9 superlayers. Five of the superlayers, in which the wires are parallel to the beam line, each is composed of the cells of 12 sense wire layers. Four of the superlayers, in which the wires are tilted by $\pm$ 3° to the beam line to provide tracking information in z axis, each is composed of the cells of 6 sense wire layers. Each cell is tilted by 45° with respect to the radial direction. Figure 2.6 shows the transverse view at the endplate of the CTC.

The momentum resolution with the combination of SVX and CTC tracking information is given by

system	η range	Energy resolution
CEM	$\lvert\eta\rvert < 1.1$	$13.7\%/\sqrt{E_T} \oplus 2\%$
PEM	$1.1 < \lvert\eta\rvert < 2.4$	$22\%/\sqrt{E} \oplus 2\%$
FEM	$2.2 < \lvert\eta\rvert < 4.2$	$26\%/\sqrt{E} \oplus 2\%$
CHA	$\lvert\eta\rvert < 0.9$	$50\%/\sqrt{E_T} \oplus 3\%$
WHA	$0.7 < \lvert\eta\rvert < 1.3$	$75\%/\sqrt{E} \oplus 4\%$
PHA	$1.3 < \lvert\eta\rvert < 2.4$	$106\%/\sqrt{E} \oplus 6\%$
FHA	$2.4 < \lvert\eta\rvert < 4.2$	$137\%/\sqrt{E} \oplus 3\%$

Table 2.1: Summary of CDF calorimeter properties. E_T is the transverse energy and E is the energy given in GeV.

$$\delta P_T / P_T = \sqrt{(0.0009 P_T)^2 + (0.0066)^2} \tag{2.2}$$

where P_T is the transverse momentum in GeV/c.

2.2.3 Calorimetry

Particles with P_T greater than 350 MeV/c are able to go out of the solenoid magnet and be detected by the calorimeters. The calorimeters are segmented in azimuth and pseudorapidity to form a projective tower geometry which points back to the nominal interaction point. They are separated into three regions in η, the central, plug, and forward. The calorimeters consist of the electromagnetic and hadronic one. The hadron calorimeter is placed outside the electromagnetic one in each region. The calorimeter properties are summarized as listed in Table 2.1.

Central calorimeter

The central electromagnetic calorimeter (CEM) covers the region of $|\eta| < 1.1$. The central hadron calorimeter (CHA) and the endwall hadron calorimeter (WHA) cover $|\eta| < 0.9$ and $0.7 < |\eta| < 1.3$ respectively. The CEM, CHA and WHA are segmented into 15° in azimuth and 0.1 in η. The CEM consists of alternative layers of a 5mm thick plastic scintillator as a sampling medium and 3mm thick lead absorber. The CEM has 31 layers of scintillator and 30 layers of lead. The CEM has the wedges segmented into 15° in azimuth. Each wedge is divided into 10 towers along the z axis. One wedge is notched to allow the access to the coil and consequently has only 8 towers. Figure 2.7 shows the perspective view of a central calorimeter wedge. The central electromagnetic shower counter (CES) is located at the CEM shower maximum to provide the shower position information in z-ϕ view. The CES is a proportional strip and wire chamber. Cathode strips running in azimuthal direction provide the z information and anode wires running in z direction provide the ϕ information. The central preradiator detector (CPR) composed of the proportional chambers is placed between the solenoid and the CEM. The CPR samples the early development of electromagnetic showers and is used to distinguish between electrons and hadrons. The CHA consists of 32 layers of a 1cm thick plastic scintillator interleaved with 2.5cm thick steel. The WHA consists of 15 layers of a 1cm thick plastic scintillator interleaved with 5cm thick steel. The CHA and WHA have 9 and 6 towers along the z axis segmented into wedge covering 15° in azimuth respectively.

The energy resolution of the CEM is $13.7\%/\sqrt{E_T} \oplus 2\%$ where $\oplus$

means adding in quadrature. The energy resolutions of the CHA and WHA are $50\%/\sqrt{E_T} \oplus 3\%$ and $75\%/\sqrt{E} \oplus 4\%$, respectively.

Plug and forward calorimeter

The plug electromagnetic calorimeter (PEM) and the plug hadron calorimeter (PHA) cover $1.1 < |\eta| < 2.4$ and $1.3 < |\eta| < 2.4$, respectively. The PEM and PHA are the gas chambers. The PEM consists of 7×7 mm^2 conductive plastic tube arrays interleaved with 2.7mm thick lead absorber. The energy resolution of the PEM is $22\%/\sqrt{E} \oplus 2\%$. The PHA consists of 14×8 mm^2 conductive plastic tube arrays interleaved with 51mm thick steel. The energy resolution of the PHA is $106\%/\sqrt{E} \oplus 6\%$. The forward electromagnetic calorimeter (FEM) and the forward hadron calorimeter (FHA) extend the η coverage up to 4.2 in $|\eta|$. The FEM and FHA consist of the gas chamber interleaved with the absorber which is lead for the FEM and steel for the FHA. The forward calorimeters are used only for the calculation of missing transverse energy ($\not\!\!E_T$).

2.2.4 Muon system

Muon system consists of three muon chambers, the central muon chamber (CMU), the central muon upgrade (CMP) and the central muon extension (CMX). All of the detectors consist of four layers of rectangular drift tubes with single wire.

Figure 2.8 shows the coverage of muon chambers. The CMU and the CMP cover 84 % and 63 % of solid angle for $|\eta| < 0.6$, respectively. And 53 % of solid angle is covered by both detectors. The CMX covers 71 % of solid angle for $0.6 < |\eta| < 1.0$.

Central muon chamber (CMU)

The central muon chamber (CMU) is located directly behind the CHA and covers $|\eta| < 0.6$. Muons with P_T above 1.4 GeV/c can reach the CMU. The CMU is divided into wedges covering 12.6 ° in azimuth. Each wedge has three towers and each tower contains four layers of four drift tubes. The outer two layers have an offset by 2mm to resolve the left-right ambiguity of track measurement in azimuth with respect to the two inner layers.

Central muon upgrade (CMP)

The central muon upgrade (CMP) reduces the background of the hadrons which "punched-through" the CMU. Muons with P_T above 2.5 GeV/c can reach the CMP. The CMP is located behind an additional steel of 0.6 m. The CMP consists of a four sided box around the CDF detector.

Central muon extension (CMX)

The central muon extension (CMX) extends the η coverage of muon chamber up to 1.0. The CMX consists of four conical arches as shown in Figure 2.3.

2.2.5 Triggers

The CDF trigger is formed by a multi-level trigger system to maximize the efficiency of the data taking of interesting events.

The CDF level 1 trigger selects events using the information of calorimeter energies and muon chamber hits. The event rate is reduced down to 1 kHz from 280 kHz by the level 1 trigger requirement.

The level 2 trigger uses the information of tracks and clustered energies. High momentum tracks using CTC hits are reconstructed using the central fast tracker (CFT) of a hardware processor. The calorimeter clusters are formed by searching for a seed tower above a certain threshold and adding neighboring towers. The level 2 output rate is $20 - 35$ Hz. The level 2 decision takes about 20 μs and incurs a dead time of a few percent.

The level 3 trigger is a software reconstruction trigger on a farm of Silicon Graphics processors. All events which pass the level 3 trigger are written to 8 mm tape. The level 3 output rate is 5-10 Hz. In this thesis we use the same triggers of a high P_T electron or muon and $\not\!\!E_T$ as in the $t\bar{t}$ events analysis [1][11].

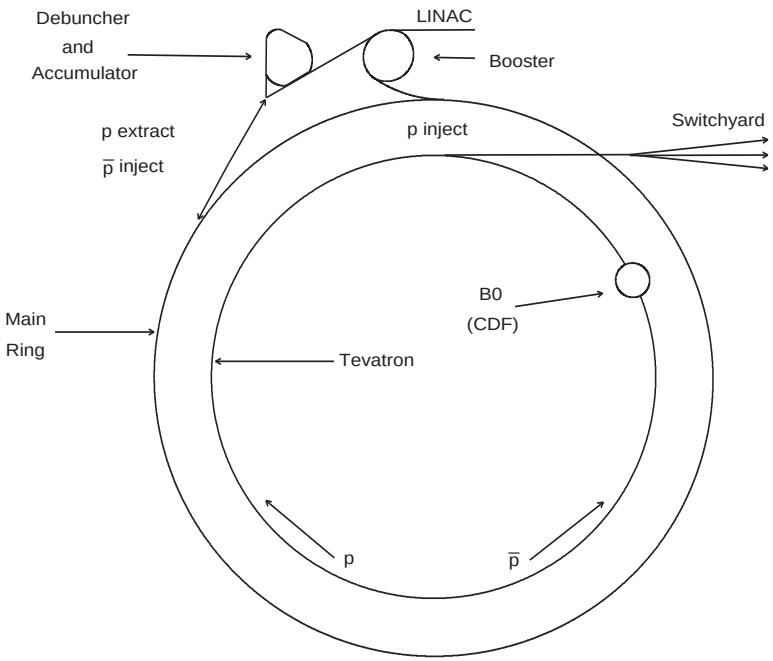

Figure 2.1: Diagram of the Tevatron accelerator complex

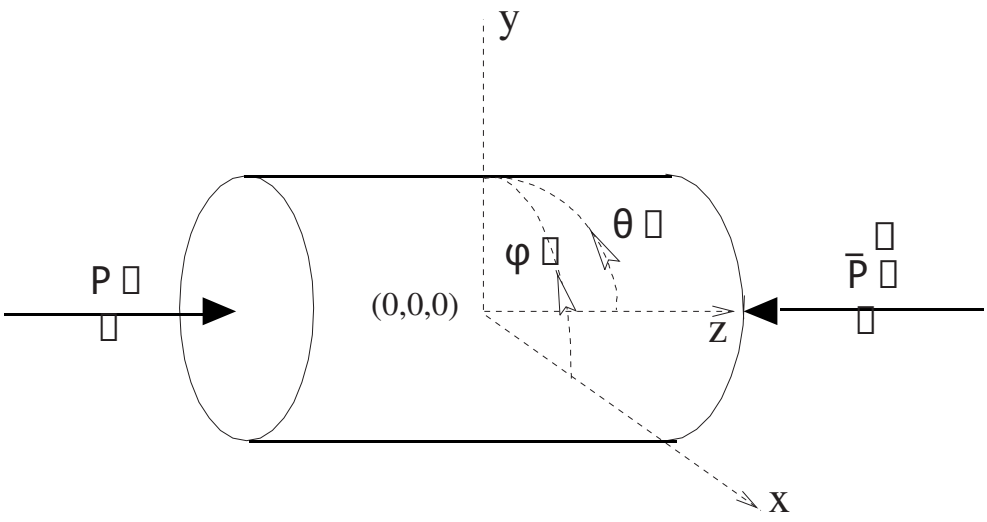

Figure 2.2: CDF coordinate system

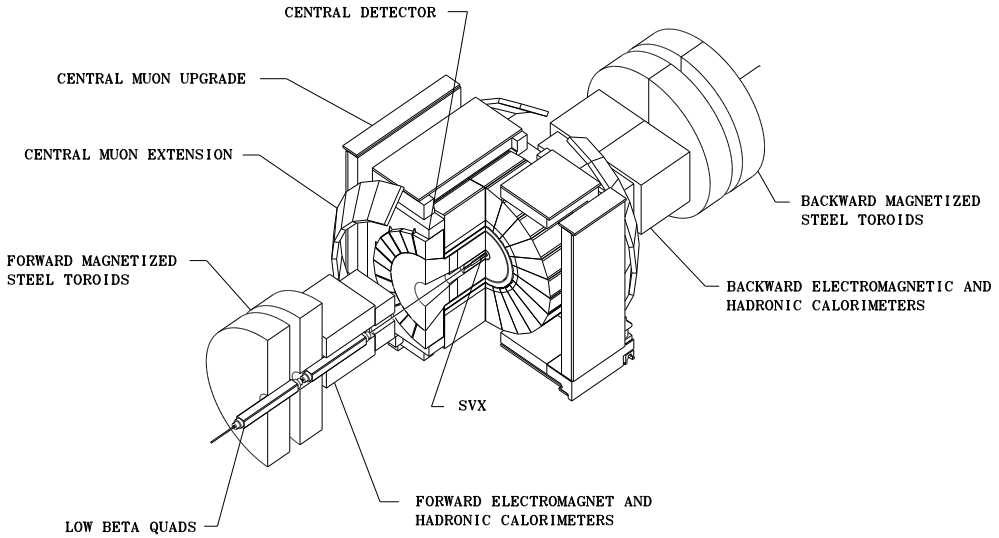

Figure 2.3: Perspective view of the CDF detector

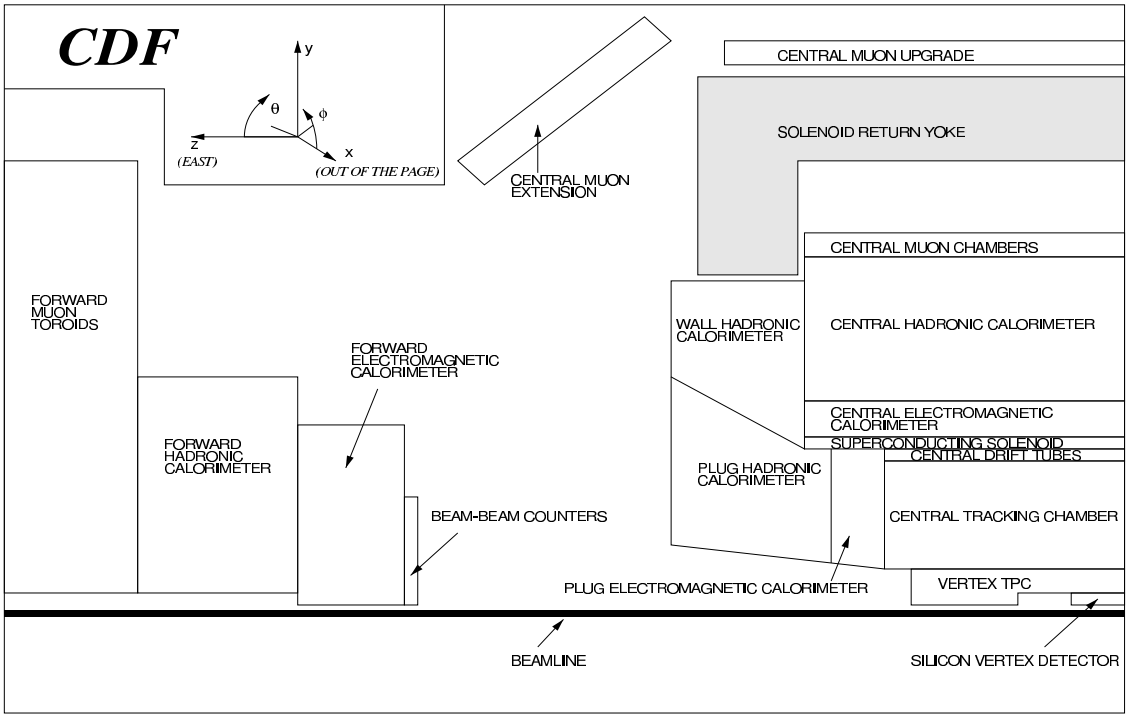

Figure 2.4: Cross-sectional view of a quadrant of the CDF detector

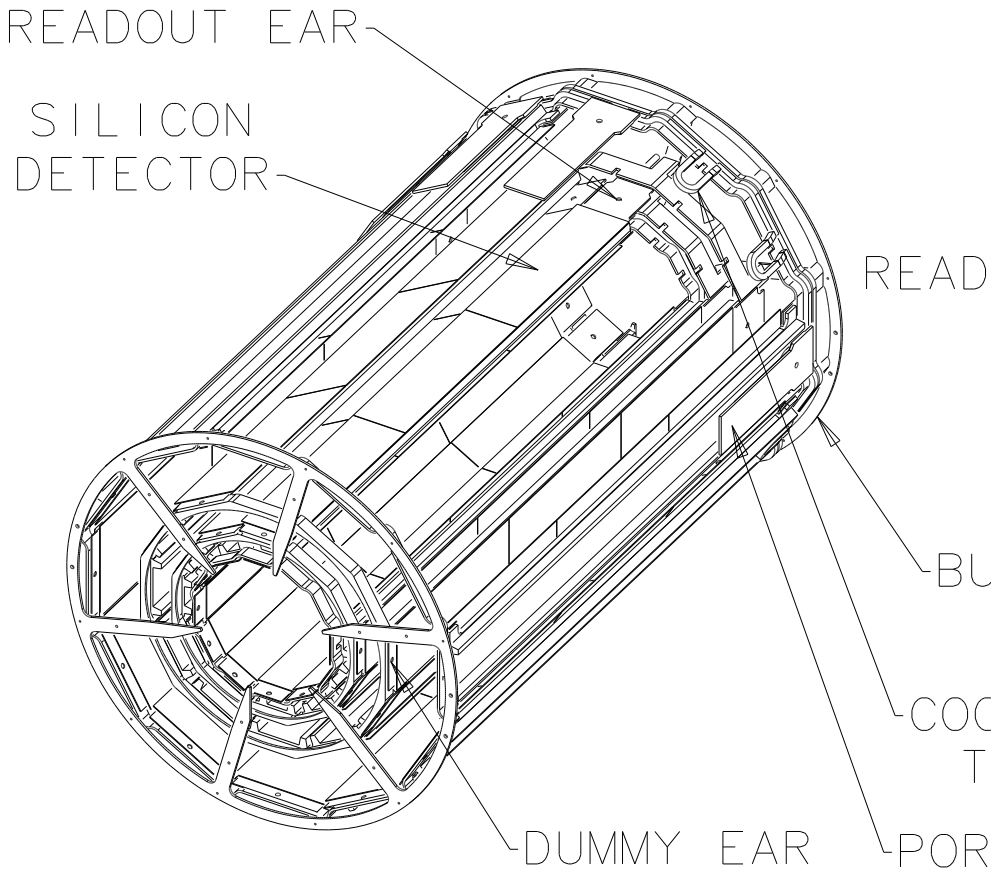

Figure 2.5: Schematic view of one barrel of the SVX detector

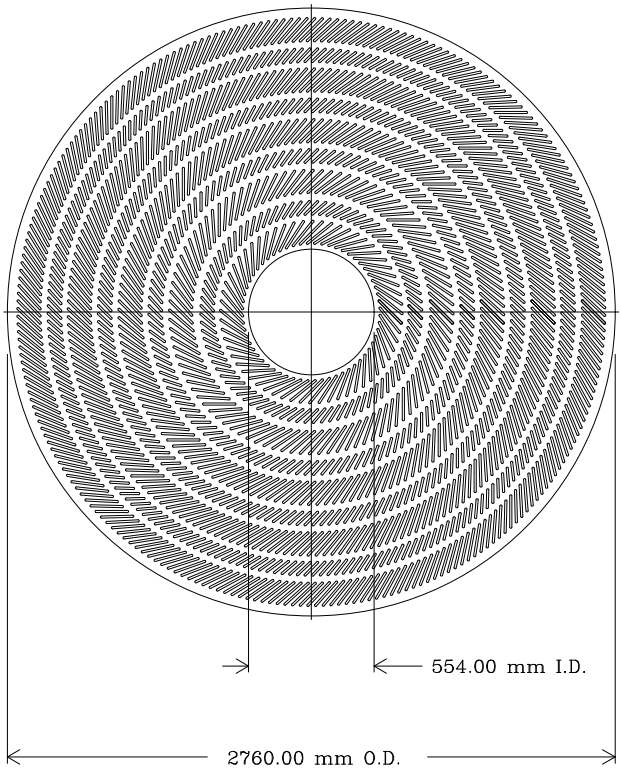

Figure 2.6: Transverse view at the endplate of the CTC showing the wire cells

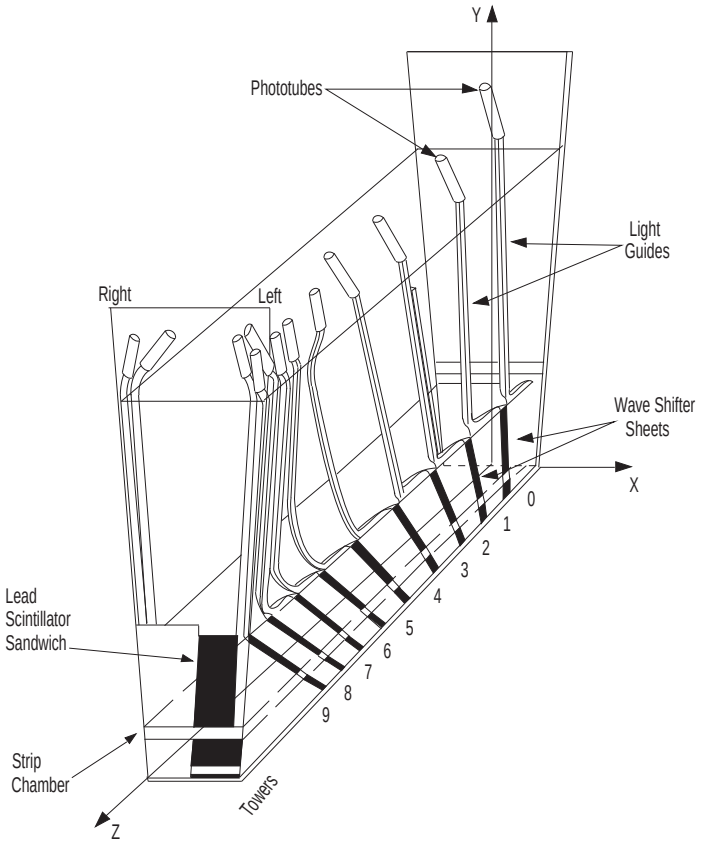

Figure 2.7: Perspective view of a central calorimeter wedge

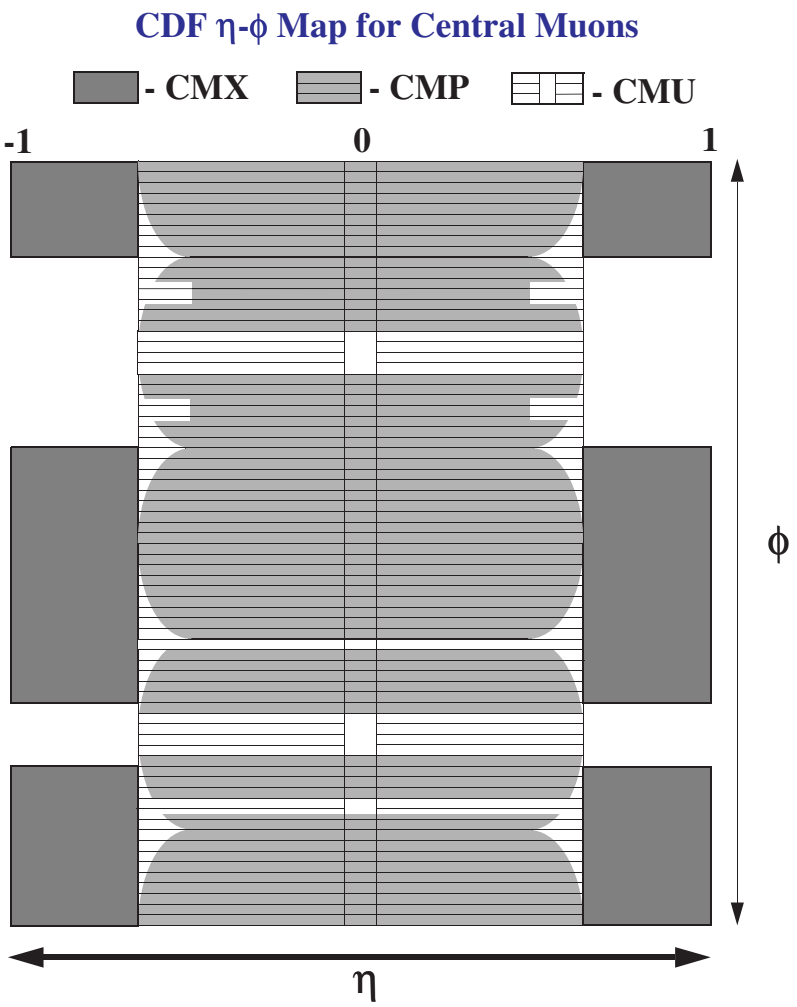

Figure 2.8: The coverage of muon chambers

Chapter 3

Event selection

We collected data corresponding to an integrated luminosity of 106.0 ± 4.1 pb^{-1} with the CDF detector in 1992-1996. In this analysis, we used this full data to select candidates events of single top quark production. The signals have a high P_T lepton, large missing transverse energy $\not\!\!E_T$ and two high E_T jets with at least one jet from b hadrons. Starting with the events which pass the level 3 trigger for high P_T electron or muon and $\not\!\!E_T$, we apply additionally selection criteria for high P_T electron or muon described in Section 3.1 and Section 3.2 and high missing transverse energy. We remove the dilepton events to reject background of Z boson production and $t\bar{t}$ production as described in Section 3.4. To suppress W+multijet events, we also require that at least one jet is identified as a jet from b-hadron.

3.1 High P_T electron selection

High P_T electron must be in the central region ($|\eta| < 1.0$) and have a CTC track pointing to an electromagnetic cluster in CEM. We apply the following cuts to the electron candidates:

- The transverse energy: $E_T > 20$ GeV.
- The ratio of the hadronic energy to the electromagnetic energy of the cluster: HAD/EM < 0.05.
- The ratio of the cluster energy to the track momentum: $E/P < 1.8$.
- A comparison of lateral shower profile in the calorimeter with that measured at test beam: Lshr < 0.2.
- The distance between the position of the extrapolated track and the CES shower position measured in the r - ϕ views: $|\Delta x| < 1.5$ cm and $|\Delta z| < 3.0$ cm.
- A χ^2 comparison of the CES shower profile with that measured at test beam: ${\chi^2}_{\rm strip} < 10$.
- The distance between the interaction vertex and the reconstructed track in the z direction: z-vertex match < 5.0 cm.
- The z position of the interaction vertex: $|z_{\rm v}| < 60$ cm.
- The ratio of $I_{\rm cal}$ to E_T of the electron cluster, where $\rm I_{cal}$ is defined as a sum of E_T's in towers within a cone of radius $R \equiv \sqrt{(\Delta\phi)^2 + (\Delta\eta)^2}$

of 0.4 centered on the electron but excluding the electron cluster E_T.

- Fiducial cut on the electron: Fiducial volume for the electron covers 84 % of the solid angle in the region $|\eta| < 1.0$.

- Photon conversion removal: If the candidate electron and other electron pass the following requirements, the candidate is removed.

  1) The difference in the cotangent of the polar angle: $|\Delta\cot\theta| < 0.06$,

  2) The separation of the two tracks at the point of tangency in r-ϕ plane: $|\Delta(r\text{-}\phi)| < 0.3$ cm, and

  3) The radial distance between the conversion point and the origin: -20 cm $< R_{conv} < 50$ cm

  or

  1) VTX occupancy < 0.2. The VTX occupancy is defined as the ratio of the number of VTX hits found to that expected. If fewer than three hits are expected, the VTX occupancy is defined to be one.

Table 3.1 lists the high P_T electron selection criteria.

3.2 High P_T muon selection

High P_T muon must have a CTC track matched to a track segment in the muon chambers and have as much energy deposition in the

$\|\eta\|$ <1.0
E_T > 20 GeV
HAD/EM < 0.05
E/P < 1.8
Lshr < 0.2
$\|\Delta x\|$ < 1.5 cm
$\|\Delta z\|$ < 3.0 cm
χ^2_{strip} < 10
z-vertex match < 5.0 cm
$\|z_{\text{v}}\|$ < 60 cm
Isolation $\text{I}_{\text{cal}}/E_T$ < 0.1
Fiducial cut on the electron
photon conversion removal

Table 3.1: Electron selection

calorimeters as a minimum ionizing particle. We apply the following cuts to the muon candidates:

- The transverse momentum: P_{T} > 20 GeV/c.
- Electromagnetic energy: EM < 2 GeV.
- Hadronic energy: HAD < 6 GeV.
- EM+HAD energy: EM + HAD > 0.1 GeV.
- The impact parameter of the reconstructed track to the beam line: D_0 < 3 mm.

- The distance between the interaction vertex and the reconstructed track in the z direction: z-vertex match < 5.0 cm.
- The z position of the interaction vertex: $|z_{\rm v}| < 60$ cm.
- Matching distance between the extrapolated track and the track segment in the muon chamber: $|\delta x| < 2$ cm for CMU hit or $|\delta x| < 5$ cm for CMP and CMX.

$\lvert\eta\rvert$ <1.0
$\mathrm{P_T} > 20$ GeV/c
EM energy < 2 GeV
HAD energy < 6 GeV
HAD+EM > 0.1 GeV
$D_0 < 3$ mm
z-vertex match < 5 cm
$\lvert z_{\rm v}\rvert < 60$cm
$\lvert\delta x\rvert < 2$ cm (CMU),< 5 cm (CMP,CMX)
Isolation $\mathrm{I_{cal}}/P_T$ <0.1

Table 3.2: Muon selection criteria

Table 3.2 lists the high P_T muon selection.

3.3 Missing transverse energy ($\not\!\!E_T$)

Neutrino is identified by a missing transverse energy ($\not\!\!E_T$) cut. The $\not\!\!E_T$ is a negative vector sum of transverse energy in all calorimeter

$E_T > 10$ GeV
E/P < 2.0 (if central)
Isolation $I_{cal}/E_T < 0.2$

Table 3.3: $Z \to ee$ second leg selection

$P_T > 10$ GeV
Isolation $I_{cal}/E_T < 0.2$

Table 3.4: $Z \to \mu\mu$ second leg selection

towers in $|\eta| < 3.6$. The thresholds of each calorimeter tower energy are 100 MeV for the CEM ,CHA and WHA, 300 MeV for the PEM and 500 MeV for the PHA and FEM, 800 MeV for the FHA. The $\not\!\!E_T$ is corrected with the muon P_T and the E_T of jets. We require that the corrected $\not\!\!E_T$ only with muon P_T is greater than 20 GeV.

3.4 Z boson production and dilepton events removal

We remove the events identified as Z boson production, Z $\to$ ee and Z $\to \mu\mu$. One leg of the Z boson decay products is the lepton identified by the selection described in Section 3.1 or Section 3.2. We require that the second leg of a Z$\to$ ee satisfies the cut in Table 3.3 and the second leg of a Z $\to \mu\mu$ satisfies the cut in Table 3.4 and the invariant mass of ee or $\mu\mu$ is between 75 and 105 GeV/c^2.

For $t\bar{t}$ background reduction, we remove the dilepton events, which have two leptons (e or μ) with $P_T > 20$ GeV/c, high $\not\!\!E_T > 25$ GeV, and two jets with $E_T > 10$ GeV [16].

We also reject dilepton events containing an isolated track with $P_T > 15$ GeV/c and a charge sign opposite to that of the primary lepton. The track isolation requirement is $\Sigma P_T < 2.0$ GeV/c in an (η, ϕ) cone of radius of 0.4 around the lepton candidate track.

3.5 Jet identification

Jets are reconstructed as an energy cluster with a cone of radius of 0.4 in η-ϕ space. First we find seed towers which E_T is greater than 1 GeV. Preclusters are formed from seed towers which is adjacent each other and the E_T weighted center of the preclusters is calculated. Then we combine towers which are in a cone of radius of 0.4 in η-ϕ space and have E_T greater than 0.1 GeV. The center of the cluster is recalculated until the set of the towers in a cluster does not change.

The jet energies may be mismeasured due to the effects, calorimeter non-linearity, out of cone losses, contributions from the underlying event, undetected energy carried by muons or neutrinos, curvature of low momentum charged particles by the CDF magnetic field, reduced calorimeter response at boundaries between modules and calorimeter subsystems. We correct the jet energies by applying the correction factors which depend on the jet E_T and η to reproduce the average jet E_T correctly, not to reduce the jet fluctuations around this mean E_T. We correct the jet transverse momentum as follows[17][18]:

$$P_T = (P_T^{raw} \times f_{rel} - M) \times f_{abs} - U + O \tag{3.1}$$

where:

- P_T^{raw} = a raw jet transverse momentum before the correction.
- f_{rel} = a correction to the η response.
- M = a correction to the underlying event of the multiple interactions.
- f_{abs} = an absolute energy scale correction.
- U = a correction to the underlying event.
- O = a correction to the out of cone losses.

Moreover we apply the jet energy correction tuned for the jets from $t\bar{t}$ decays, which is extracted by comparing the measured jet momentum and parton momenta before detector simulation on $t\bar{t}$ Monte Carlo[1] events.

We require exactly two jets with uncorrected $E_T > 15$ GeV and $|\eta| < 2.0$. Figure 3.1 shows the multiplicity distribution of jets with uncorrected $E_T > 15$ GeV and $|\eta| < 2.0$ for single top events simulated using HERWIG Monte Carlo event generator and detector simulation. We will describe the Monte Carlo simulation in Section 3.7.

3.6 B-tagging

B-tagging is the identification of a jet from a b quark. There are two b-tagging methods. Secondary vertex tagging (SVX) and soft lepton

tagging (SLT). We use the SVX method as a primary b-tagging. The SLT method is used to detect the second b-jet in double b-tagged events which have two b-tagged jets.

3.6.1 SVX b-tagging algorithm

The SVX b-tagging utilizes the long decay length due to the long life time of b hadrons. We first form a secondary vertex with three or more good tracks with two or more SVX hits and $P_T > 0.5$ GeV/c. For the candidate of secondary vertex, we require $\frac{L_{xy}}{\sigma_{L_{xy}}} > 3.0$ and $|L_{xy}| < 2.5$ cm. L_{xy} and $\sigma_{L_{xy}}$ are the two dimensional decay length in x-y plane and its measurement error, respectively, as shown in Figure 3.2. L_{xy} has a sign which is defined as cosine of the angle between the jet momentum direction and the direction to the decay point from the collision point. We require L_{xy} to be positive. If the candidate does not pass the cut, we form a secondary vertex and with two or more good tracks which has three or four SVX hits and $P_T > 1.0$ GeV/c apply the same cuts as above.

3.6.2 SLT b-tagging algorithm

The soft lepton tagging (SLT) algorithm searches for leptons produced in the b quark decays through $b \to l\nu$X or $b \to c \to l\nu$X. These leptons do not have a high P_T and are called soft leptons. We select the soft lepton track which has $P_T > 2$ GeV/c and $|\eta| < 1$ and of which direction is within a cone radius of 0.4 around the axis of the jet and $\frac{L_{xy}}{\sigma_{L_{xy}}} > 2$. The detail of the SLT tagging is described in [11] and [19]. If a jet has the soft electron or muon, it is defined as a b-tagged jet.

3.7 Monte Carlo simulations

To model the signal and background events we use Monte Carlo programs. HERWIG Monte Carlo program [20][21] is our primary modeling of the signal events. HERWIG is based on the leading order QCD matrix elements followed by parton shower evolution. The W-gluon fusion process is simulated with the process $q+b \to q'+t$. We use PYTHIA [22][23] as an another modeling of the signal events. PYTHIA is also based on the leading oder QCD matrix elements, but partons are fragmented using Lund string model instead of parton shower evolution. VECBOS [25] is a parton-level Monte Carlo program based on tree-level matrix element calculation. VECBOS is used for a modeling of the W+jets background events. CLEOMC is used in all Monte Carlo generator for the b-hadron decays [24]. The CDF detector simulation called QFL' is performed after the event generation.

3.8 Signal acceptance for W+2 jet events

The signal acceptance is calculated with Monte Carlo samples. We correct the difference in the efficiency between the Monte Carlo samples and the data for the lepton identification and b-tagging. The decay of a W boson from a top quark is forced to $e\nu$ or $\mu\nu$ in the simulation. We apply a data/MC scale factor of 0.94 for the lepton identification efficiency. This scale factor was estimated from a comparison between the lepton identification efficiency for $Z^0 \to \ell\ell$ events in the data and that for $W + \geq 1$ jet events in HERWIG Monte Carlo.

We also apply a data/MC scale factor of 1.0 ± 0.1 for the SVX b-

tagging efficiency. The number of reconstructed tracks for the data is smaller than Monte Carlo. We extracted this scale factor by taking ratio of the b-tagging efficiency with degrading the track reconstruction efficiency to that without degrading it in the simulation.

The scale factor for the SLT tagging efficiency is 0.95 ± 0.05. The signal acceptance and the expected number of events are listed in Table 3.5. The expected number of SVX b-tagged W+2jet signal events is 1.2 ± 0.2 for the W-gluon fusion process and 1.8 ± 0.3 for the s-channel W^* process. We will describe the method to estimate the uncertainty on the acceptance in Sections 4.3.2 and 5.4.2. We checked the contribution from $W \rightarrow \tau\nu$ events to the W+2jet SVX b-tagged events using Monte Carlo simulation and found it to be negligible. They are 0.11 events for the W-gluon fusion process and 0.05 events for the s-channel $W^\star$ process.

	s-channel W^*	W-gluon fusion
σ_{theory} (pb)	0.73 ± 0.10	1.7 ± 0.3
Luminosity (pb^{-1})	106.0 ± 4.1	106.0 ± 4.1
W+2jet cut acceptance (%)	3.4 ± 0.5	3.3 ± 0.6
SVX b-tag efficiency (%)	44.6 ± 4.5	29.5 ± 3.0
SVX b-tagged events expected	1.2 ± 0.2	1.8 ± 0.3
Double b-tag efficiency(%)	11.9 ± 1.3	0.6 ± 0.06
Double b-tagged events expected	0.31 ± 0.05	0.04 ± 0.05

Table 3.5: The expected numbers of events for single-top production through the s-channel W^* and W-gluon fusion processes.

3.9 Expected background and observed data

Dominant backgrounds in the W + 2jet SVX b-tagged events are $t\bar{t}$, Mistags, $Wb\bar{b}$, $Wc\bar{c}$ and Wc. The expected number of background events in the CDF W+jets data is reported in the references [11] and [19]. We estimate the number of $t\bar{t}$ background events with the CDF $t\bar{t}$ production cross section of $6.5^{+1.7}_{-1.4}$ pb [28] and the acceptance using HERWIG and PYTHIA Monte Carlo. The estimated $t\bar{t}$ background is 5.7 ± 1.3 events.

The mistags occur from the fluctuation of the secondary vertices due to the errors of the track reconstruction in the light quark jets. The mistag rate per jet is calculated from the tagging rate with negative impact parameter L_{xy} in the generic jet sample where most jets are light quark jets. We apply the mistag rate to the data and extract the number of mistag events to be 6.3 ± 2.6.

For the $Wb\bar{b}$+$Wc\bar{c}$ background estimation, we first normalize the number of events in the simulation to the number of W + 2 jet events before b-tagging in the CDF data which is 1,527. From the the W + 2 jet events we subtract the non-W background events estimated from the lepton isolation and $\not\!\!E_T$ as described in detail later in this section. Then using Monte Carlo simulation, we estimate the b-tagging efficiencies and the fraction of $Wb\bar{b}$ and $Wc\bar{c}$ production in the W+jets events after subtracting non-W background. The expected $Wb\bar{b}$+$Wc\bar{c}$ background is 9.0 ± 2.5 events. The Wc background is also estimated in the same way as $Wb\bar{b}$+$Wc\bar{c}$ background. The expected Wc background is 4.3 ± 1.5 events. The $Zb\bar{b}$ and $Zc\bar{c}$ backgrounds where $b\bar{b}$ or $c\bar{c}$ comes from gluon splitting are estimated in the same way as the $Wb\bar{b}$ and $Wc\bar{c}$ backgrounds.

We take into account the $gg \rightarrow Zb\bar{b}$ background. The expected Z+heavy flavor background is 0.7 ± 0.3 events. The diboson production backgrounds, WW and WZ, are calculated with the theoretical cross sections and the acceptance from PYTHIA Monte Carlo simulation. The cross section from theory is 9.5 ± 0.7 pb for WW and 2.6 ± 0.4 pb for WZ [26] [27]. The expected diboson background is 1.4 ± 0.5 events. We extract the contribution from the non-W production background using the lepton isolation and $\not\!\!E_T$. We divide a two-dimensional plane of the Isolation vs $\not\!\!E_T$ into the following four regions:

- region A: $\not\!\!E_T < 15GeV$, Isolation < 0.1
- region B: $\not\!\!E_T < 15GeV$, Isolation > 0.2
- region C: $\not\!\!E_T > 20GeV$, Isolation > 0.2
- region D: $\not\!\!E_T > 20GeV$, Isolation < 0.1 (signal region)

Since the Isolation and $\not\!\!E_T$ are uncorrelated with each other, the non-W background in the signal region is extracted from $\frac{A \times C}{B}$. We estimate the non-W background to be 2.3 ± 1.0 events.

Table 3.6 lists the expected number of background events. We estimate the total background to be 29.8 ± 4.7 events in the SVX b-tagged W + 2jet events and observe 42 events.

Source	B-tagged events		
QCD backgrounds:			
Mistags	6.3 ± 2.6		
$Wb\bar{b}$+$Wc\bar{c}$	9.0 ± 2.5		
Wc	4.3 ± 1.5		
Z+heavy flavor	0.7 ± 0.3		
Dibosons	1.4 ± 0.5		
Non-W	2.3 ± 1.0	single b-tagged	double b-tagged
Total QCD backgrounds	24 ± 4.5	22.4 ± 4.5	1.6 ± 0.4
$t\bar{t}$ background	5.7 ± 1.3	4.7 ± 1.3	1.0 ± 0.25
W-gluon fusion	1.8 ± 0.3	1.8 ± 0.3	0.04 ± 0.05
s-channel $W^{\star}$	1.2 ± 0.2	0.9 ± 0.2	0.3 ± 0.05
Total expected	32.7 ± 4.7	29.8 ± 4.7	2.9 ± 0.5
Observed	42	36	6

Table 3.6: Expected and observed numbers of SVX b-tagged W+2jet events.

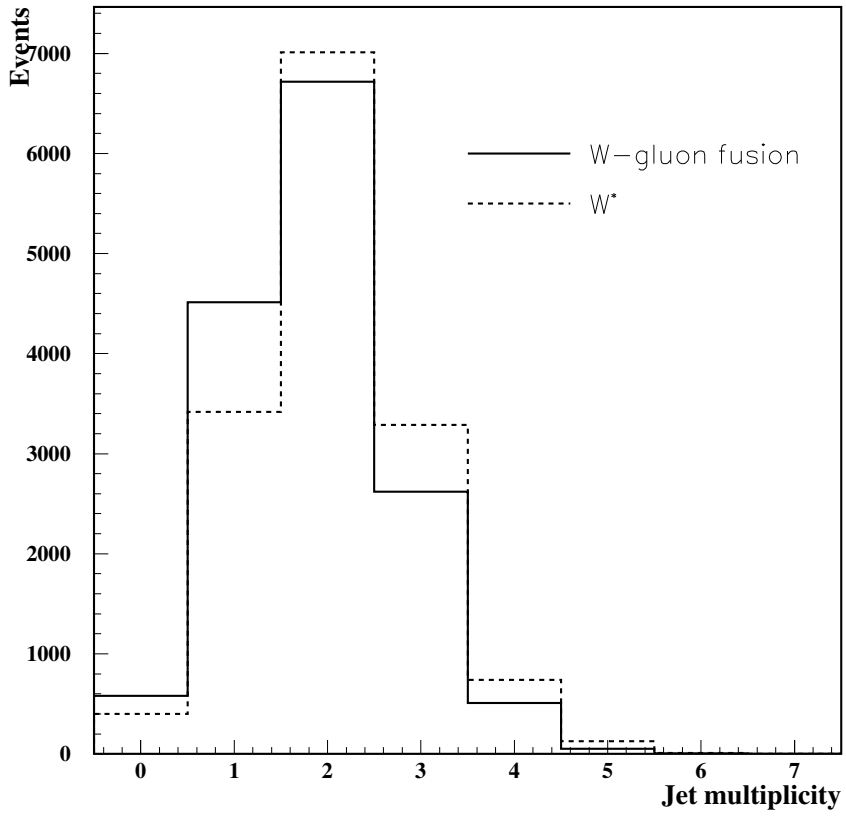

Figure 3.1: Jet multiplicity distribution with uncorrected $E_T > 15$ GeV and$|\eta| < 2.0$.

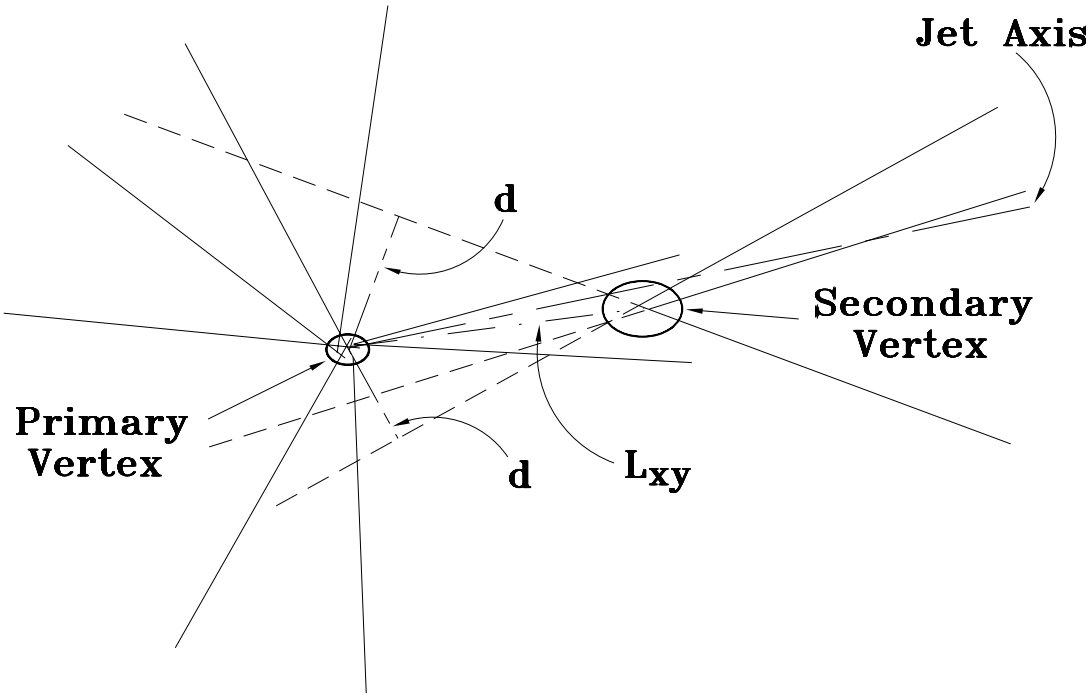

Figure 3.2: Cross section view of an event containing a secondary vertex

Chapter 4

Search for single top quark production through the W-gluon fusion process

We start with the sample of W + 2jet events with at least one SVX b-tagged jet. The W-gluon fusion signal has only one b-jet leading two jets in the because another bottom quark coming from gluon splitting is soft. Figure 4.1 shows the P_T distribution before hadronization for the HERWIG signal events. We remove double b-tagged events and apply a reconstructed top mass cut. There is no ambiguity in assigning a jet to the b-jet from a top quark decay in leading two jets after removing the double b-tagged events. Finally we perform a likelihood fit of the distribution of the product of the lepton charge and the untagged jet pseudorapidity, Q$\times\eta$.

4.1 Reconstructed top mass window cut

We reconstruct the top quark mass using the four-momenta of the lepton (e or μ), the ν and the b-tagged jet. For the neutrino P_z we take the solution with the smallest absolute value from the W-mass constraint. If the solution is a complex number, we use its real part. Figures 4.2 show the reconstructed top mass distributions for the CDF data, HERWIG Monte Carlo simulation of single top in the W-gluon fusion channel, HERWIG single top in the W^* channel, VECBOS $Wb\bar{b}$, HERWIG $t\bar{t}$ and PYTHIA Wc. The reconstructed top mass distributions for PYTHIA WW, PYTHIA WZ and VECBOS Zbb are shown in Figure 4.3.

We check the reconstructed top mass distribution for the events where the b-jet is correctly assigned to the jet from top quark decay in single top events. We compare the direction of the jet momentum vector before the quark fragmentation with the direction of the b-tagged jet used in top mass reconstruction. If the two directions are close to each other by less than 0.4 in $\eta - \phi$ space, we take the b-jet as a correctly assigned b-tagged jet. Figures 4.4 (a) and (b) show the reconstructed top mass distribution for W-gluon fusion single top and s-channel W^* single top events, respectively. Solid histograms show the single b-tagged events and hatched histograms show the events with the right b-jet assignment. 92% and 49% of the events are correctly assigned in the W-gluon fusion process and s-channel W^* process, respectively.

In Table 4.1 we list the expected number of events and the $S/\sqrt{B}$ after the top mass window cut as a function of the mass window. To calculate the top mass cut efficiency, we use VECBOS for $Wb\bar{b}$, $Wc\bar{c}$ and $Zb\bar{b}$, HERWIG for $t\bar{t}$, and PYTHIA for Wc and dibosons (WW,WZ). We

use a VECBOS $Wb\bar{b}$ sample to estimate the background due to mistags, $Wc\bar{c}$ and non-W. In the table, the QCD label includes all backgrounds except for the $t\bar{t}$ background. The optimal top mass window is from 145 to 205 GeV/c^2. The total acceptance for the signal is 0.85 $\pm$ 0.24%.

We observe fifteen data events after the top mass window cut, while we expect a total background of 13.1$\pm$2.1 events and a signal of 1.4$\pm$0.3 events.

	Expected number of events				
	Wg	W^*	QCD	$t\bar{t}$	S/$\sqrt{B}$
no cut	1.8	1.2	24.0	5.7	0.323
double tag removal	1.8	0.9	22.4	4.7	0.334
130-220	1.6	0.7	15.4	2.9	0.372
135-215	1.6	0.7	13.8	2.7	0.378
140-200	1.5	0.6	12.0	2.4	0.384
145-205	1.4	0.6	10.2	2.2	0.387
150-200	1.3	0.5	8.4	1.9	0.383
155-195	1.1	0.4	6.7	1.6	0.370
160-190	0.9	0.3	5.0	1.2	0.340

Table 4.1: Expected number of events and $S/\sqrt{B}$ for several top mass window cuts. The QCD background includes all backgrounds except for the $t\bar{t}$ background.

4.2 Likelihood fit of $Q \times \eta$ distribution

The pseudorapidity of the light quark jet tends to be positive for single top quark production and negative for the $\bar{t}$ production[29]. The quark in the initial state of the top quark (not $\bar{t}$) production through the W-gluon fusion process is a u or $\bar{d}$ quark in the first generation (Figure 4.5). Since the initial parton density of u or $\bar{d}$ in the proton (the valence quarks are uud) is greater than in the antiproton, the light quark from the proton is more than that from the antiproton in the top production. Since the momentum transfer between the initial light quark and the final light quark is not large, the light quark from u or $\bar{d}$ in the top production tends to go to proton direction. In the same way, the light quark in the $\bar{t}$ production tends to go to the antiproton direction. For using this asymmetry, we make the distribution of the product of the lepton charge Q and the untagged jet pseudorapidity η. Figure 4.6 shows the Q$\times\eta$ distributions for the CDF data and Monte Carlo simulation. We perform a binned maximum likelihood fit of this distribution. The likelihood is defined as follows:

$$L(\mu_{t\bar{t}}, \mu_{QCD+W^*}, \mu_{Wg}) = \frac{e^{-\frac{1}{2}\left(\frac{\mu_{t\bar{t}} - n_{t\bar{t}}}{\Delta_{t\bar{t}}}\right)^2}}{\sqrt{2\pi}\Delta_{t\bar{t}}} \times \frac{e^{-\frac{1}{2}\left(\frac{\mu_{\mathrm{QCD+W^*}} - n_{\mathrm{QCD+W^*}}}{\Delta_{\mathrm{QCD+W^*}}}\right)^2}}{\sqrt{2\pi}\Delta_{\mathrm{QCD+W^*}}}$$

$$\times \prod_i \frac{e^{-\mu_i} \cdot \mu_i^{n_i}}{n_i!} \tag{4.1}$$

where:

- $\mu_{t\bar{t}}$, μ_{QCD+W^*}, μ_{Wg} = fit parameters representing, respectively, the numbers of $t\bar{t}$, QCD+W^* and Wg events in the CDF data.

- n_{QCD+W^*}, $n_{t\bar{t}}$ = expected numbers of events from QCD+W^* and $t\bar{t}$, respectively ($n_{QCD+W^*} = 10.9$, $n_{t\bar{t}} = 2.2$).

- Δ_{QCD+W^*}, $\Delta_{t\bar{t}}$ = uncertainties on the expected numbers of events from QCD+W^* and $t\bar{t}$, respectively ($\Delta_{QCD+W^*} = 2.0$, $\Delta_{t\bar{t}} = 0.6$).

- $\mu_i = \mu_{QCD+W^*} \cdot \alpha_i + \mu_{t\bar{t}} \cdot \beta_i + \mu_{Wg} \cdot \gamma_i$, where α_i, β_i and γ_i are the expected fractions of QCD+W^*, $t\bar{t}$ and Wg events in the i-th bin.

- n_i = observed number of events in the i-th bin of the Q×η distribution.

We use a $Wb\bar{b}$ Monte Carlo sample to model the QCD background. The likelihood fit is performed under the background constraint provided by the Gaussian factors in the likelihood function. The fit result is given in Table 4.2 and the fitted Q×η distribution is shown in Figure 4.7. The fitted number of signal events is consistent with theory and also with zero.

Table 4.3 shows the fit result without the background constraints. The number of W-gluon fusion signal and $t\bar{t}$ background are forced to be positive. Since we do not observe any significant single top events through W-gluon fusion process, we set an upper limit on its cross section.

4.3 Systematic uncertainty

Systematic uncertainties can affect both the acceptance of our event selection and the shape of the Q×η distribution. So we estimate both uncertainties.

	input	fitted
QCD+W^*	10.9 $\pm$ 2.0	11.0 $\pm$ 1.9
$t\bar{t}$	2.2 $\pm$ 0.6	2.2 $\pm$0.6
Wg	free	$1.3^{+4.2}_{-1.3}$

Table 4.2: Parameter input and output values for the fit of the Q$\times\eta$ distribution with background constraints.

	fitted
QCD +W^*	15.0 $^{+4.2}_{-11.6}$
$t\bar{t}$	0.0 $^{+9.4}_{-0.0}$
Wg	0.0 $^{+6.7}_{-0.0}$

Table 4.3: Parameter input and output values for the fit of the Q$\times\eta$ distribution without background constraints.

4.3.1 Systematic uncertainty on the shape

We perform pseudo-experiments to estimate the systematic uncertainty on the shape. At first we make standard HERWIG Monte Carlo simulation to have the Q$\times\eta$ distributions which are called standard templates. For each source of systematic uncertainty we rerun our top and background Monte Carlo events after shifting the corresponding parameter by one standard deviation (or some reasonable estimate thereof) to have the Q$\times\eta$ distributions which are called shifted templates. In each pseudo-experiment we fluctuate the number of background events and signal events according to a Poisson statistics. If the total number of

events is equal to fifteen, we take them as the number of events in the pseudo-experiment. We generate Q×η value of each event according to the standard Q×η distribution template. We perform a likelihood fit of the Q×η distribution to a sum of standard signal and background templates with a fitting parameter of the relative number of signal events α, i.e. the ratio of the fitted number of signal events to the number predicted by theory. We make 20,000 pseudo-experiments generated from the standard signal and background templates. We take a median of α as $\alpha_{standard}$. Next we perform a likelihood fit of the Q×η distribution to a sum of shifted signal and background templates for each pseudo-experiments, and take a median of α as $\alpha_{shifted}$. We then define the corresponding systematic uncertainty on α as the difference between $\alpha_{standard}$ and $\alpha_{shifted}$.

We consider the following systematic uncertainties on the shape of the $Q \times \eta$ distribution:

- Monte Carlo generator

  We use the PYTHIA as the different Monte Carlo model. and take the difference between HERWIG and PYTHIA as the systematic uncertainty. The relative number of signal events is 1.53 for HERWIG and 1.61 for PYTHIA. We take the symmetrized difference, $\pm$0.08, as systematic uncertainty.

- Initial state radiation (ISR)

  We use PYTHIA to study the effect of gluon radiation, which has the option to tune on or off the initial state radiation. We take half the difference between PYTHIA without initial state radiation and

standard PYTHIA. The relative number of signal events is 1.46 for PYTHIA-noISR and 1.61 for standard PYTHIA, leading to a systematic uncertainty of ± 0.08.

- Final state radiation (FSR)

  We take half the difference between PYTHIA-noISR and PYTHIA-noISR where the two jets match the partons within a cone of 0.4 in η-ϕ space. The parton four momenta are those in the generator level of PYTHIA before hadronization and the detector simulation. The relative number of signal events is 1.46 for PYTHIA-noISR and 1.51 for PYTHIA-noISR with parton-jet matching. The corresponding systematic uncertainty is ± 0.03.

- Parton distribution functions (PDF)

  We are using parton distribution function MRSD_' [30] as the standard in Monte Carlo signal event generation. We take CTEQ4L [31] as the different parton distribution model and symmetrize the difference between MRSD_' and CTEQ4L as the systematic uncertainty. The relative number of signal events is 1.42 for CTEQ4L and 1.53 for MRSD_', resulting in a systematic uncertainty of ± 0.11.

- Background modeling

  Our standard QCD background model is VECBOS $Wb\bar{b}$. As alternate model we combine PYTHIA Wc and VECBOS $Wb\bar{b}$ in the ratio Wc:Wbb=3:7. The relative number of signal events is 1.53 for the standard background and 1.52 for the alternate model. We take the symmetrized difference, ± 0.01, as systematic uncertainty.

Figure 4.8 shows the Q×η distributions for HERWIG Monte Carlo signal events (standard), PYTHIA Monte Carlo with systematic shift, PYTHIA with no initial state radiation, PYTHIA with no initial state radiation with parton -jet matching and HERWIG with parton distribution of CTEQ4L. Table 4.4 lists the systematic uncertainties on the shape. The total uncertainty on the shape is 0.16 in the relative number of signal events.

Systematic	Absolute uncertainty on the ratio of fitted signal to theory prediction
Parton distributions	± 11 %
Signal generator	± 8 %
Initial state radiation	± 8 %
Final state radiation	± 3 %
Background model	± 1 %
Total	± 16 %

Table 4.4: Systematic uncertainties affecting the shape of the $Q \times \eta$ distribution.

4.3.2 Systematic uncertainty on the acceptance

Table 4.5 shows the systematic uncertainty on the acceptance. we assigned 10% uncertainty on the trigger and the lepton ID efficiencies since we use simulations to extract the efficiencies. The uncertainty on

the b-tagging efficiency also comes from the the difference between Monte Carlo and data. We shift the jet energy positively and negatively by hand to evaluate jet energy scale effects. The uncertainty due to the jet energy scale is less than 1%, essentially because shifts of events between the 1-jet and 2-jet bins are compensated by shifts of similar size between the 2-jet and 3-jet bins (see Figure 5.6). We take half the difference between the acceptances with positively and negatively shifted corrections as systematic uncertainty. For the uncertainties due to signal generator, initial state radiation, final state radiation and parton distribution, we extract the acceptances with Monte Carlo sample by shifting the corresponding parameter and take the difference in the same way as for the uncertainty on the shape.

Systematic	Relative uncertainty
Trigger+lepton ID	± 10 %
B-tagging	± 10 %
Signal generator	± 9 %
Initial state radiation	± 7 %
Final state radiation	± 7 %
Luminosity	± 4 %
Parton distributions	± 1 %
Jet energy scale	± 1 %
Total	± 20 %

Table 4.5: Systematic uncertainties affecting the acceptance.

4.4 Cross section limit

We use the binned likelihood in equation (4.1) to set an upper limit on the cross section of single top production through the W-gluon fusion process. We take the same procedure that was used to extract a limit on $t\bar{t}$ production cross section from the 1988-1989 data [32]. First, we calculate the likelihood $L(\alpha)$ of a given relative number of signal events α by maximizing $L(\mu_{t\bar{t}}, \mu_{QCD+W^*}, \alpha)$ with respect to $\mu_{t\bar{t}}$ and μ_{QCD+W^*}. Next we smear $L(\alpha)$ with a Gaussian to include the effect of systematic uncertainties:

$$L'(\alpha) \equiv \int_0^\infty L(x) \times G(x; \alpha, \sigma(x))\, dx \ , \tag{4.2}$$

where α is the relative number of signal events and $G(x; \alpha, \sigma(x))$ is a normalized Gaussian distribution with a mean α and a width $\sigma(x)$:

$$\sigma(x) = \sqrt{\sum_{i=1}^{9} (\Delta_i + x\delta_i)^2} \tag{4.3}$$

Δ_i is the absolute uncertainty on the shape and δ_i is the relative uncertainty on the acceptance of the Q$\times\eta$ distribution from the i-th systematic source. Table 4.6 shows Δ_i and δ_i. The sign indicates the direction of the systematic shift. The 95% C.L. upper limit $\alpha_{\text{U.L.}}$ satisfies the following equation:

$$\int_0^{\alpha_{\text{U.L.}}} L'(\alpha)\, d\alpha \ = \ 0.95 \times \int_0^\infty L'(\alpha)\, d\alpha \tag{4.4}$$

Figure 4.9 shows $L'(\sigma)$ as a function of the cross section σ ($\sigma = \alpha \times 1.7$ pb). We extract 13.5 pb as the 95% C.L. upper limit on the cross section.

If the systematic uncertainties are not taken into account, the 95% C.L. upper limit on the production cross section becomes 12.5 pb (using $L(\alpha)$ instead of $L'(\alpha)$).

	i	Δ_i	δ_i
MC generator	1	$+0.08$	-0.09
ISR	2	-0.03	$+0.07$
FSR	3	$+0.03$	-0.07
Jet energy scale	4	0.0	-0.01
PDF	5	-0.11	-0.01
Luminosity	6	0.0	$+0.04$
B-tagging	7	0.0	$+0.10$
Trigger+lepton ID	8	0.0	$+0.10$
background	9	-0.01	0.0

Table 4.6: The absolute uncertainty on the shape Δ_i and the relative uncertainty on the acceptance δ_i

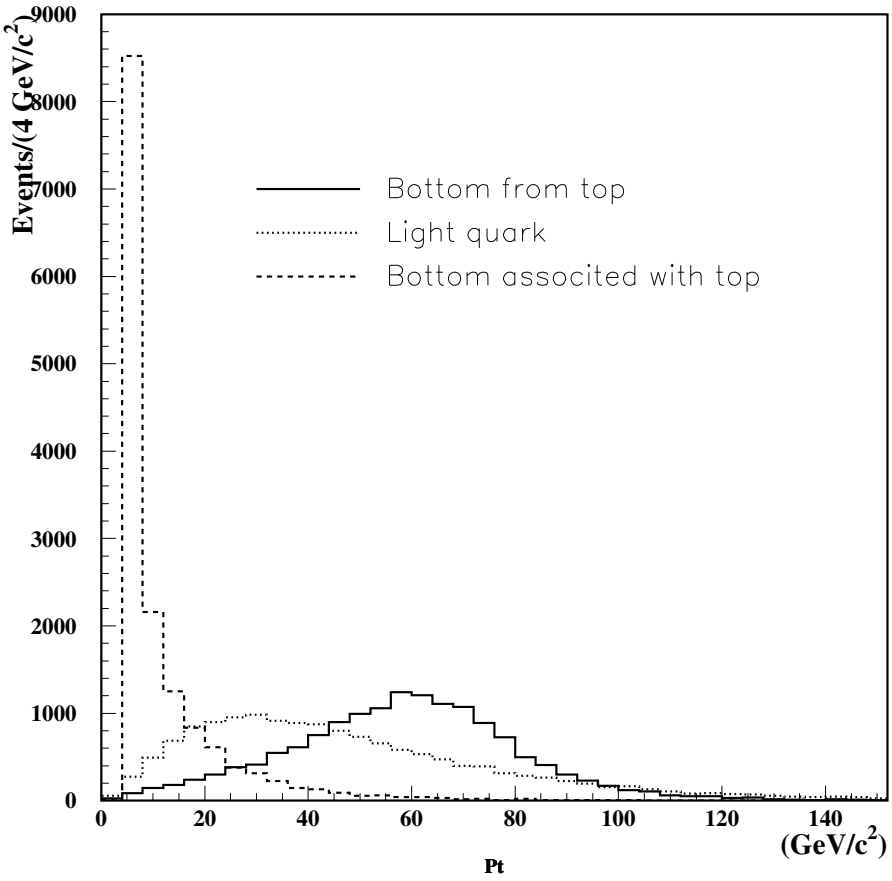

Figure 4.1: P_T distribution for the W-gluon fusion single top events with HERWIG Monte Carlo.

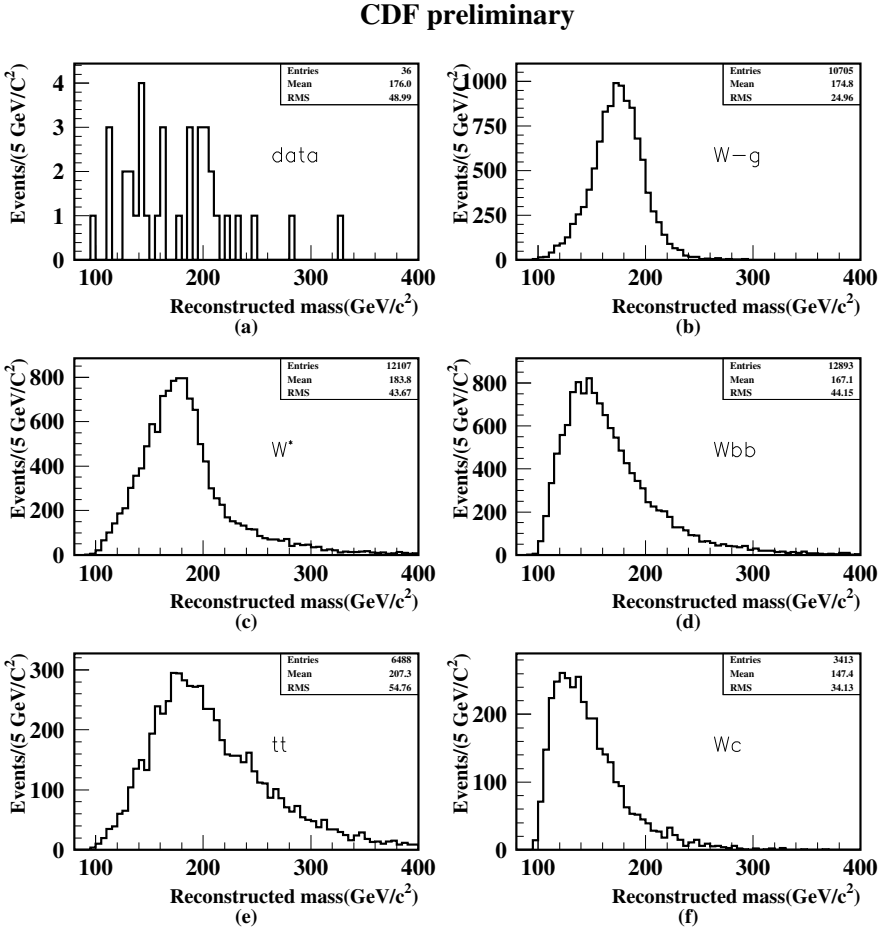

Figure 4.2: Reconstructed top mass distributions for data (a), single top events through the W-gluon fusion process (b), single top events through the s-channel W^* channel (c), VECBOS $Wb\bar{b}$ (d), HERWIG $t\bar{t}$ (e) and PYTHIA Wc (f).

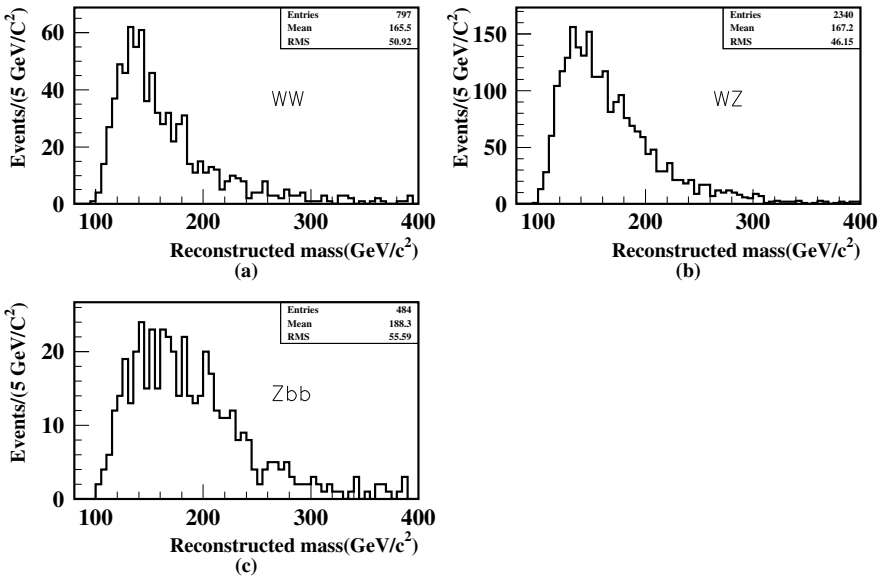

Figure 4.3: Reconstructed top mass distributions for PYTHIA WW (a), PYTHIA WZ (b), VECBOS Zbb (c).

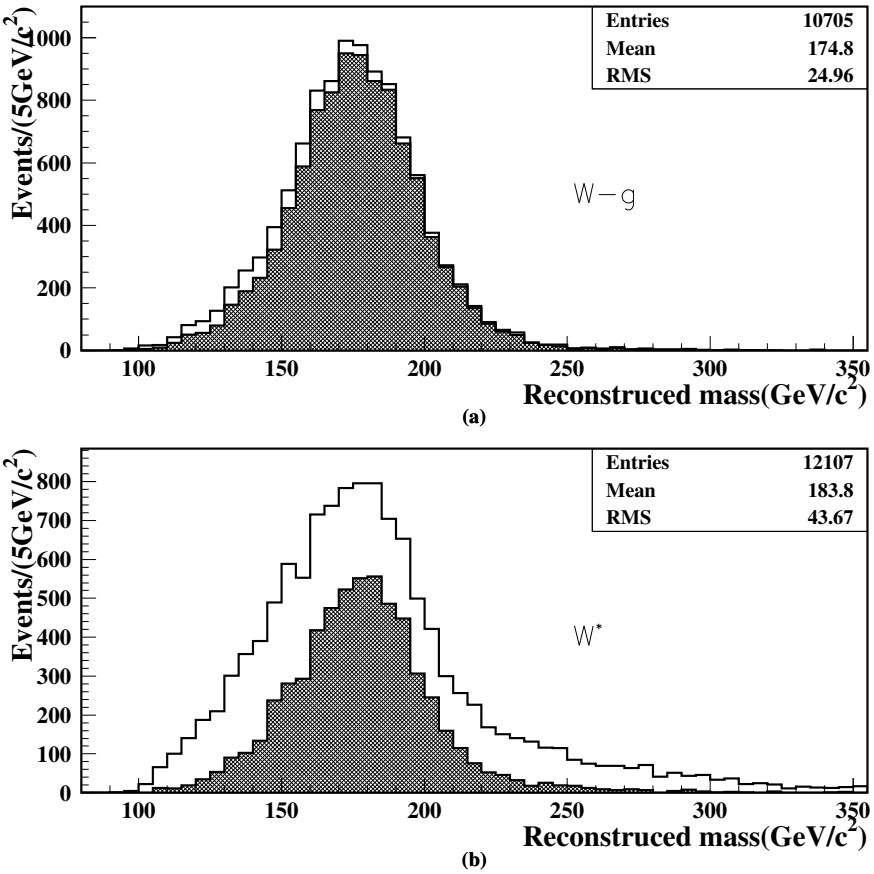

Figure 4.4: Reconstructed top mass distributions for single top events through the W-gluon fusion process (a) and single top events through the s-channel W^* process (b). Hatched histograms show the events with the right b-jet assignment.

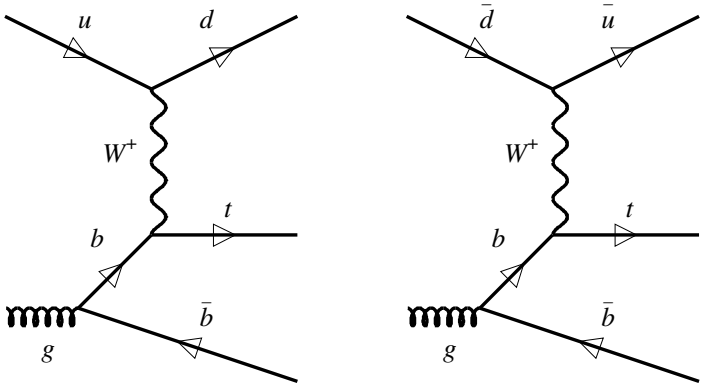

Figure 4.5: Diagrams for single top quark production through W-gluon fusion processes with top (not $\bar{t}$) quark.

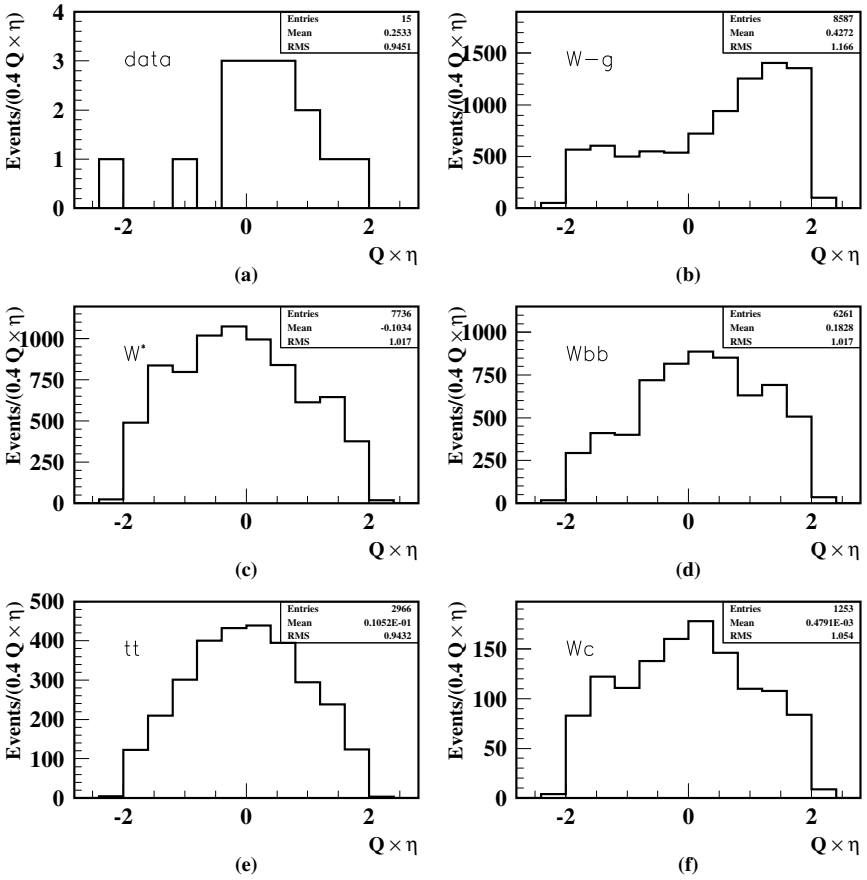

Figure 4.6: Q×η distributions for data (a), single top events through the W-gluon fusion process (b), single top events through the s-channel W^* process (c), VECBOS $Wb\bar{b}$ (d), HERWIG $t\bar{t}$ (e) and PYTHIA Wc (f).

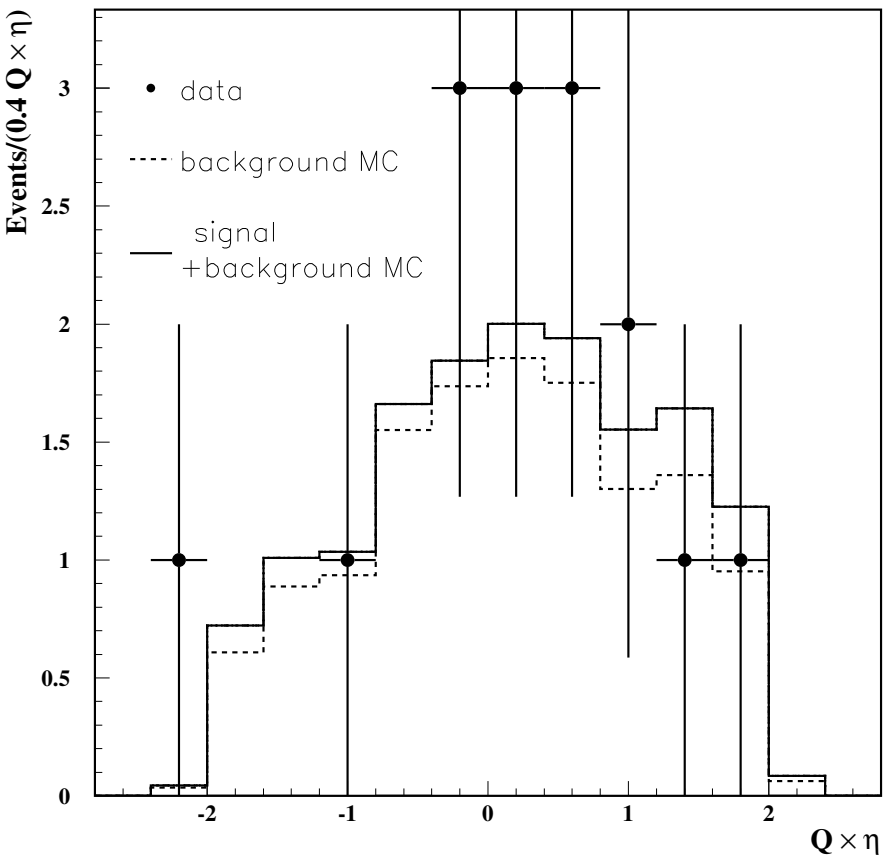

Figure 4.7: Fitted Q×η distribution. The points show the CDF data, the dashed histogram shows the fitted background, and the solid histogram shows the fitted signal plus background.

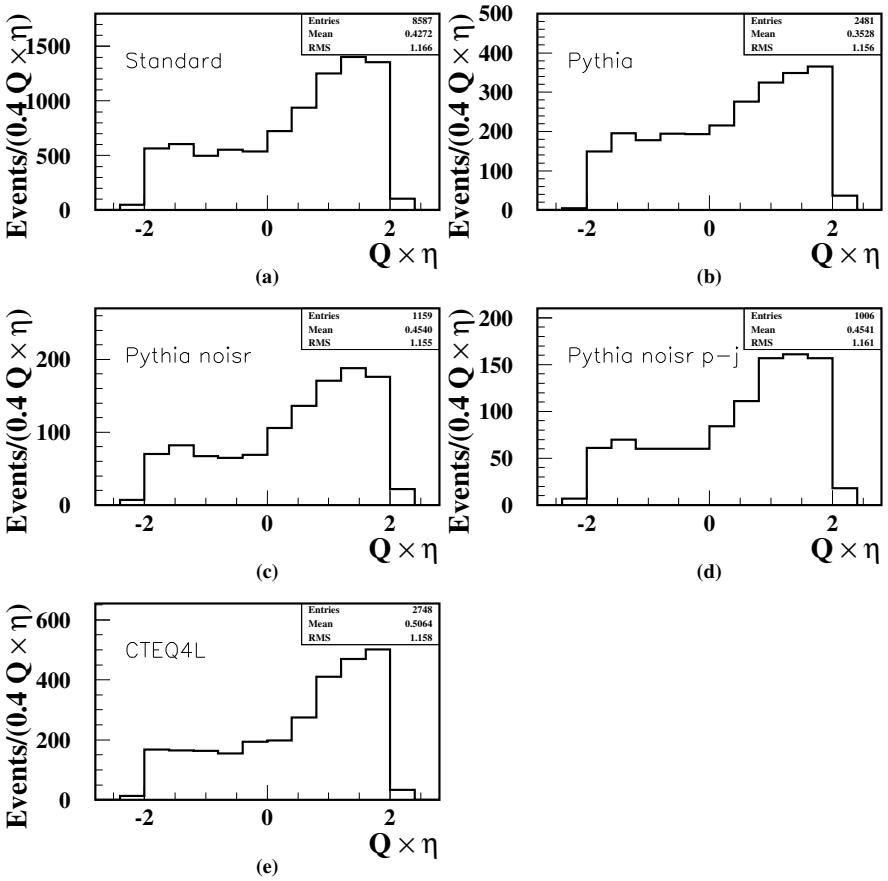

Figure 4.8: Q×η distributions for the standard HERWIG signal events with MRSD_' parton distribution (a), PYTHIA Monte Carlo signal events with systematic shift (b), PYTHIA without initial state radiation (c), PYTHIA without initial state radiation and with parton -jet matching (d), and HERWIG signal events with CTEQ4L parton distribution (e).

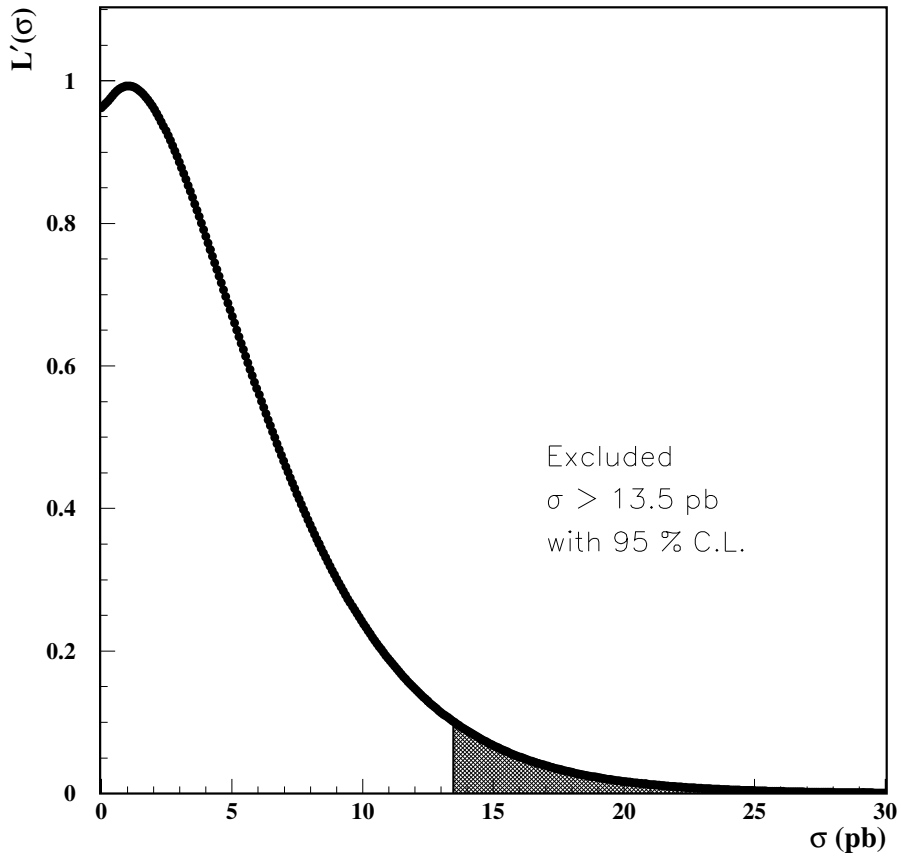

Figure 4.9: Smeared likelihood $L'(\sigma)$ as a function of the cross section of single top production through the W-gluon fusion process for the CDF data.

Chapter 5

Search for single top quark production through the s-channel W^* process

Signal detection of single top production through s-channel W^* process is more difficult than that through W-gluon fusion process. Reconstructed top mass is the best distribution to distinguish between the signal and the background. We reconstruct the top mass from a W bosn and a jet in the W + 2 jet events with at least one SVX b-tagged jet. Then we perform a likelihood fit of the top mass distribution to obtain an upper limit on the cross section.

5.1 Top mass reconstruction

We reconstruct the top mass using the four-momenta of the lepton (e or μ), ν and one of the jets. The assignment of b-jets is different

from the top mass reconstruction in the search for single top production through W-gluon fusion process. Since a b-jet from a top quark decay tends to go along the proton direction[33], we define a jet with larger η as the b-jet from the top quark. For $\bar{t}$ events we define a jet with smaller η as the $\bar{b}$-jet from $\bar{t}$ quark. For the neutrino P_z we take the solution with the smallest absolute value from the W-mass constraint. If the solution is a complex number, we use its real part.

The reconstructed top mass distributions for data and Monte Carlo are shown in Figures 5.1 and 5.2. Figures 5.3 (a) and (b) show the reconstructed top mass distribution for single top events through W-gluon fusion process and s-channel W^* process, respectively. Solid histograms show the events with single b-tagged and hatched histograms show the events with the right b-jet assignment. 36% and 64% of the events have correctly assigned b-jet in the W-gluon fusion and s-channel W^* single top events, respectively.

5.2 Cross section limit from predicted and observed event rates

At first we use Poisson statistics to extract a 95% C.L. upper limit on the cross section in the s-channel W^* process. We observe 42 b-tagged W+2jet events in the data while we expect 31.5 ± 4.7 background events. The uncertainty on the W^* acceptance is 17%.

The 95% C.L. upper limit on the signal events u is extracted from:

$$\sum_{i=0}^{N} \sum_{j=0}^{i} \left(\int_0^\infty G(x; \mu_b, \sigma_b) P(x; j) dx \right) \left(\int_0^\infty G(x; u, \sigma_u) P(x; i-j) dx \right)$$

$$= 0.05 \times \sum_{i=0}^{N} \int_0^{\infty} G(x; \mu_b, \sigma_b) P(x, i) dx \tag{5.1}$$

where

- u, σ_u = 95% C.L. upper limit on the number of signal events and its uncertainty ($\sigma_u = 0.15 \times u$).
- μ_b, σ_b = the expected number of background events and its uncertainty, respectively.
- N = the number of observed events(N=42).
- $G(x; \mu_b, \sigma_b)$ =a Gaussian probability for variable x with mean μ_b and width σ_b.
- $P(x; j)$ = a Poisson probability for value j with mean x.

From this equation we extract an upper limit of 27.3 events. After dividing by the W^* acceptance (1.52%) and the luminosity (106 pb^{-1}), we obtain an upper limit of 16.9 pb.

This limit can be improved by applying a top mass window cut. To optimize the window size, we calculate $S/\sqrt{B}$. In this calculation we use VECBOS to model $Wb\bar{b}$ and $Zb\bar{b}$ backgrounds, HERWIG for $t\bar{t}$, and PYTHIA for Wc and dibosons (WW,WZ). We also assume that the VECBOS $Wb\bar{b}$ sample is an adequate model for mistags, $Wc\bar{c}$ and non-W events.

The optimal top mass window is from 135 to 215 GeV/c^2. The efficiency of this cut for W^* events is 79%. Twenty five events survive this cut while total expected background is 19.3$\pm$2.7 events. The uncertainty on the W^* acceptance is 15%. From this we extract a 95% C.L. upper limit of 18.0 events, or 13.9 pb.

5.3 Likelihood fit of the reconstructed mass distribution

5.3.1 Binned likelihood fit

We perform a binned maximum likelihood fit using the top mass distribution. We define the likelihood as follows:

$$L(\mu_{t\bar{t}+Wg}, \mu_{QCD}, \mu_{W^*}) = \frac{e^{-\frac{1}{2}\left(\frac{\mu_{t\bar{t}+\mathrm{Wg}} - n_{t\bar{t}+\mathrm{Wg}}}{\sigma_{t\bar{t}+\mathrm{Wg}}}\right)^2}}{\sqrt{2\pi}\sigma_{t\bar{t}+\mathrm{Wg}}} \times \frac{e^{-\frac{1}{2}\left(\frac{\mu_{\mathrm{QCD}} - n_{\mathrm{QCD}}}{\sigma_{\mathrm{QCD}}}\right)^2}}{\sqrt{2\pi}\sigma_{\mathrm{QCD}}}$$

$$\times \prod_i \frac{e^{-\mu_i} \cdot \mu_i^{n_i}}{n_i!} \tag{5.2}$$

where

- $\mu_{t\bar{t}+Wg}$, μ_{QCD}, μ_{W^*} = fit parameters representing, respectively, the numbers of $t\bar{t} + Wg$, QCD and W^* events in the data.
- n_{QCD}, $n_{t\bar{t}+Wg}$ = expected numbers of events from QCD and $t\bar{t}+Wg$ respectively ($n_{QCD} = 24.0$, $n_{t\bar{t}+Wg} = 7.5$).
- σ_{QCD}, $\sigma_{t\bar{t}+Wg}$ = uncertainties on the expected numbers of events from QCD and $t\bar{t} + Wg$ respectively ($\sigma_{QCD} = 4.5$, $\sigma_{t\bar{t}+Wg} = 1.3$).
- $\mu_i = \mu_{QCD} \cdot \alpha_i + \mu_{t\bar{t}+Wg} \cdot \beta_i + \mu_{W^*} \cdot \gamma_i$, where α_i, β_i and γ_i are the expected fractions of QCD, $t\bar{t} + Wg$ and W^* events that enter bin i.
- n_i = observed number of events in the i-th bin of the reconstructed top mass distribution.

We use a $Wb\bar{b}$ Monte Carlo sample to model the QCD background. The fit result is given in Table 5.1 and the fitted top mass distribution is shown in Figure 5.4. The fitted number of signal events is consistent with the number of events expected from theory. It is also about one standard deviation away from zero.

Table 5.2 shows the fit result without the background constraints provided by the Gaussian factors in the likelihood function. The W^* signal is forced to be positive. If we do not force the signal to be positive, we obtain the results listed in Table 5.3.

Since we do not observe single top production through s-channel W^* process, we will set an upper limit on its cross section.

	input	output
QCD	24.0 ± 4.5	$25.7\ ^{+4.2}_{-4.1}$
$t\bar{t}+Wg$	7.5 ± 1.3	7.6 ± 1.3
W^*	free	$6.4^{+7.3}_{-6.4}$

Table 5.1: Parameter input and output values for the binned likelihood fit of the reconstructed top mass distribution with background constraints.

5.3.2 Unbinned likelihood fit

We also tried an unbinned likelihood fit to check the likelihood method. We define the unbinned likelihood as follows:

$$L(\mu_{t\bar{t}+Wg}, \mu_{QCD}, \mu_{W^*}) = \frac{e^{-\frac{1}{2}\left(\frac{\mu_{t\bar{t}+Wg} - n_{t\bar{t}+Wg}}{\sigma_{t\bar{t}+Wg}}\right)^2}}{\sqrt{2\pi}\sigma_{t\bar{t}+Wg}} \times \frac{e^{-\frac{1}{2}\left(\frac{\mu_{\mathrm{QCD}} - n_{\mathrm{QCD}}}{\sigma_{\mathrm{QCD}}}\right)^2}}{\sqrt{2\pi}\sigma_{\mathrm{QCD}}}$$

	output
QCD	$33.8\ ^{+11.1}_{-10.3}$
$t\bar{t}+Wg$	$8.2\ ^{+9.7}_{-8.2}$
W^*	$0.0\ ^{+10.7}_{-0.0}$

Table 5.2: Parameter output values for the binned likelihood fit of the reconstructed top mass distribution without background constraints, but forcing the parameters to be positive.

	output
QCD	$35.6\ ^{+13.2}_{-11.7}$
$t\bar{t}+Wg$	$10.6\ ^{+13.9}_{-11.6}$
W^*	$-4.2^{+14.3}_{-14.1}$

Table 5.3: Parameter output values for the binned likelihood fit of the reconstructed top mass distribution without background constraints and without forcing the parameters to be positive.

$$\times \prod_i \frac{\mu_{QCD} f_{QCD}(m_i) \ + \ \mu_{t\bar{t}+Wg} f_{t\bar{t}+Wg}(m_i) \ + \ \mu_{W^*} f_{W^*}(m_i)}{\mu_{QCD} \ + \ \mu_{t\bar{t}+Wg} \ + \ \mu_{W^*}} \quad (5.3)$$

where

- n_{QCD}, $n_{t\bar{t}+Wg}$ = expected number of events from QCD and $t\bar{t}+Wg$ respectively ($n_{QCD} = 24.0$, $n_{t\bar{t}+Wg} = 7.5$).

- σ_{QCD}, $\sigma_{t\bar{t}+Wg}$ = uncertainty on the expected number of events from QCD and $t\bar{t}+Wg$ respectively ($\sigma_{QCD} = 4.5$, $\sigma_{t\bar{t}+Wg} = 1.3$).

- μ_{QCD}, $\mu_{t\bar{t}+Wg}$, μ_{W^*} = fitted numbers of events from QCD, $t\bar{t}+Wg$ and W^* respectively.

- $f_{QCD}(m_i)$, $f_{t\bar{t}+Wg}(m_i)$, $f_{W^*}(m_i)$ = probability densities for a reconstructed top mass m_i for an event from QCD, $t\bar{t}+Wg$ and W^* respectively.

The fit results are listed in Tables 5.4 (with background constraints) and 5.5 (without background constraints). The fitted number of events with this unbinned likelihood fit is very close to the one with the binned likelihood fit.

	input	output
QCD	24.0 ± 4.5	$25.4\ ^{+4.2}_{-4.1}$
$t\bar{t}+Wg$	7.5 ± 1.3	7.6 ± 1.3
W^*	free	$7.0^{+7.3}_{-6.7}$

Table 5.4: Parameter input and output values for the unbinned likelihood fit with background constraints.

	output
QCD	$32.9\ ^{+11.0}_{-10.8}$
$t\bar{t}+Wg$	$9.1\ ^{+9.7}_{-9.1}$
W^*	$0.0\ ^{+12.4}_{-0.0}$

Table 5.5: Parameter output values for the unbinned likelihood fit without background constraints.

5.4 Systematic uncertainty

5.4.1 Systematic uncertainty on the shape of the reconstructed mass distribution

We estimate systematic uncertainty on the shape of the reconstructed mass distribution from 20,000 pseudo-experiments. We have the following systematic uncertainties on the shape of the reconstructed mass distribution:

- Monte Carlo generator

  The relative number of signal events is 8.07 for HERWIG and 7.36 for PYTHIA. We take the symmetrized difference, ± 0.71, as systematic uncertainty.

- Initial state radiation (ISR)

  The relative number of signal events is 7.00 for PYTHIA-noISR and 7.36 for standard PYTHIA, leading to a systematic uncertainty of ± 0.18.

- Final state radiation (FSR)

  The relative number of signal events is 7.00 for PYTHIA-noISR and 6.62 for PYTHIA-noISR with parton-jet matching. The corresponding systematic uncertainty is ± 0.19.

- Parton distribution function (PDF)

  The relative number of signal events is 7.96 for CTEQ4L and 8.07 for MRSD_', resulting in a systematic uncertainty of ± 0.11.

- Jet energy scale

  We take the same method to estimate this systematic uncertainty as the top mass measurement at CDF[34][35]. The following systematic uncertainties are calculated with Equation 3.1 in Section 3.5:

  - Calorimeter stability = 1 % of P_T^{raw}.
  - Relative correction = 0.2 to 4 % of f_{rel}.
  - Correction to the underlying event of multiple interactions = 100 MeV.
  - Absolute correction = 2.5 %
  - Soft gluon radiation = 1.4 %
  - Splash-out beyond cone of 0.1 = 1 GeV.

  We add all systematic uncertainty in quadrature. We shifted the extracted energy by hand to evaluate jet energy scale effects. The relative number of signal events is 7.52 for positive shifts and 8.19 for negative shifts. We take half the difference between the two as systematic uncertainty, i.e. ± 0.34.

- Background uncertainty

  Our standard QCD background model is VECBOS $Wb\bar{b}$. As alternate model we combine PYTHIA Wc and VECBOS $Wb\bar{b}$ in the ratio Wc:Wbb=3:7. The relative number of signal events is 8.07 for the standard background and 7.83 for the alternate model. We take the symmetrized difference, ± 0.25, as systematic uncertainty.

Figure 5.5 shows the reconstructed top mass distributions for s-channel W^* signal events generated with standard PYTHIA Monte Carlo, PYTHIA with no initial state radiation, PYTHIA with no initial state radiation and parton-jet matching, HERWIG with parton distribution of CTEQ4L, HERWIG with positively shifted jet energy and with negatively shifted jet energy. Table 5.6 lists the systematic uncertainties on the shape. The total uncertainty on the shape is 0.87 in the relative number of signal events.

CDF preliminary

Systematic	Absolute uncertainty on the ratio of fitted signal to theory prediction
Signal generator	± 71 %
Jet energy scale	± 34 %
Background model	± 25 %
Final state radiation	± 19 %
Initial state radiation	± 18 %
Parton distributions	± 11 %
Total	± 87 %

Table 5.6: Systematic uncertainties affecting the shape of the reconstructed top mass distribution.

5.4.2 Systematic uncertainty on the acceptance

Table 5.7 shows the systematic uncertainty on the acceptance. The uncertainties are estimated in the same way as at the search for single top production through W-gluon fusion process. Jet energy scale uncertainty does not change the acceptance so much because it does not change the jet multiplicity distribution as shown in Figure 5.6. The total systematic uncertainty on the acceptance is 15%.

CDF preliminary

Systematic	Relative uncertainty
Trigger+lepton ID	$\pm$ 10 %
B-tagging	$\pm$ 10 %
Signal generator	$\pm$ 6 %
Initial state radiation	$\pm$ 6 %
Luminosity	$\pm$ 4 %
Final state radiation	$\pm$ 4 %
Parton distributions	$\pm$ 2 %
Jet energy scale	$< \pm$ 1 %
Total	$\pm$ 17 %

Table 5.7: Systematic uncertainties affecting the acceptance.

5.5 Cross section limit

We use the binned likelihood in equation (5.2) to set an upper limit on the single top production cross section through the s-channel

W^* process. We calculate the likelihood $L(x)$ in the same way as the W-gluon fusion single top search and smear $L(x)$ with a Gaussian to include the effect of systematic uncertainties:

$$L'(\alpha) = \int_0^\infty L(x) \times G(x; \alpha, \sigma(x))\, dx \ , \tag{5.4}$$

where α is the relative number of signal events and $G(x; \alpha, \sigma(x))$ is a normalized Gaussian distribution with mean α and width $\sigma(x)$:

$$\sigma(x) = \sqrt{\sum_{i=1}^{9} (\Delta_i + x\delta_i)^2} \tag{5.5}$$

Δ_i is the absolute uncertainty on the shape and δ_i is the relative uncertainty on the acceptance of the reconstructed top mass distribution from the i-th systematic source. Table 5.8 shows Δ_i and δ_i. The sign indicate the direction of the systematic shift. The 95% C.L. upper limit $\alpha_{\text{U.L.}}$ satisfies the following equation:

$$\int_0^{\alpha_{\text{U.L.}}} L'(\alpha)\, d\alpha \ = \ 0.95 \times \int_0^\infty L'(\alpha)\, d\alpha \tag{5.6}$$

Figure 5.7 shows $L'(\sigma)$ as a function of the cross section σ ($\sigma = \alpha \times 0.73$ pb). We extract 12.9 pb as a 95 % C.L. upper limit on the cross section. Note that this upper limit is better than that obtained from Poisson statistics (section 5.2) since it makes use of the shape information.

If the systematic uncertainties are not taken into account, the 95% C.L. upper limit on the production cross section becomes 12.4 pb (using $L(\alpha)$ instead of $L'(\alpha)$).

5.6 Checks of the likelihood method

We checked the likelihood method by running various types of pseudo-experiments.

	i	Δ_i	δ_i
MC generator	1	-0.71	-0.06
ISR	2	-0.18	-0.06
FSR	3	-0.19	$+0.04$
Jet energy scale	4	-0.34	$+0.01$
PDF	5	-0.10	$+0.02$
Luminosity	6	0.0	$+0.04$
B-tagging	7	0.0	$+0.10$
Trigger+lepton ID	8	0.0	$+0.10$
Background	9	-0.25	0.0

Table 5.8: The absolute uncertainty on the shape Δ_i and the relative uncertainty on the acceptance δ_i

5.6.1 Check of the likelihood fit

We generate 20,000 samples consisting of N_b background and N_s signal events each, where N_b is a Poisson fluctuation of the number of events given in Table 3.6 and N_s is a Poisson fluctuation of the fit result (6.6 events). We fit each sample using our binned-likelihood method. Figure 5.8 shows the distribution of the fitted number of signal events and the corresponding pulls which is the deviation of the fitted number of signal events from 6.6 events divided by the error of the fit number of signal events. The mean fitted number of signal events is 6.6, and its RMS is 6.8. The pulls distribution has a mean of 0.0 and a width of 1.0.

5.6.2 Check of the upper limit calculations

We generate another 20,000 samples of N_b background and N_s signal events each, where N_b is again a Poisson fluctuation of the number of events given in Table 5.1, but N_s is a Poisson fluctuation of the unsmeared 95% C.L. upper limit on the signal. We fit each sample using our binned-likelihood method. Figure 5.9 shows the distribution of the fitted number of signal events. The fitted number of signal events is equal to or less than 6.6 events in 3.5% of the pseudo-experiments.

All our tests with pseudo-experiments show that our likelihood procedures behave as expected.

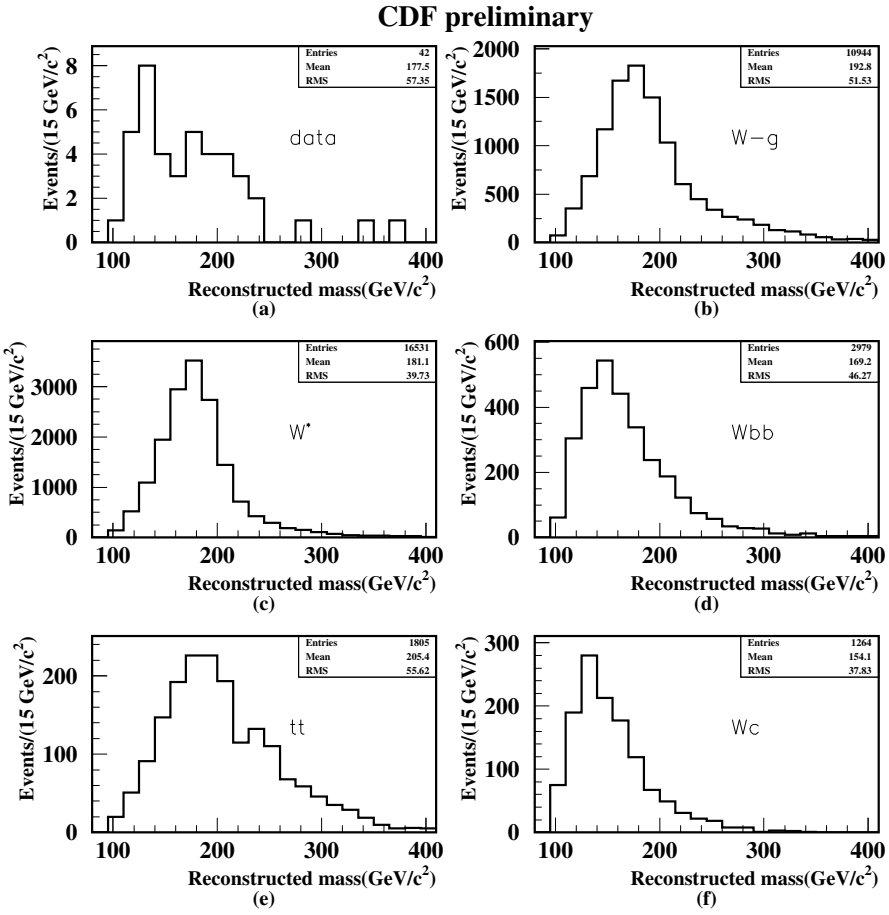

Figure 5.1: Reconstructed top mass distributions for data (a), single top through the W-gluon fusion process (b), single top through the W^* process (c), VECBOS $Wb\bar{b}$ (d), HERWIG $t\bar{t}$ (e), and PYTHIA Wc (f).

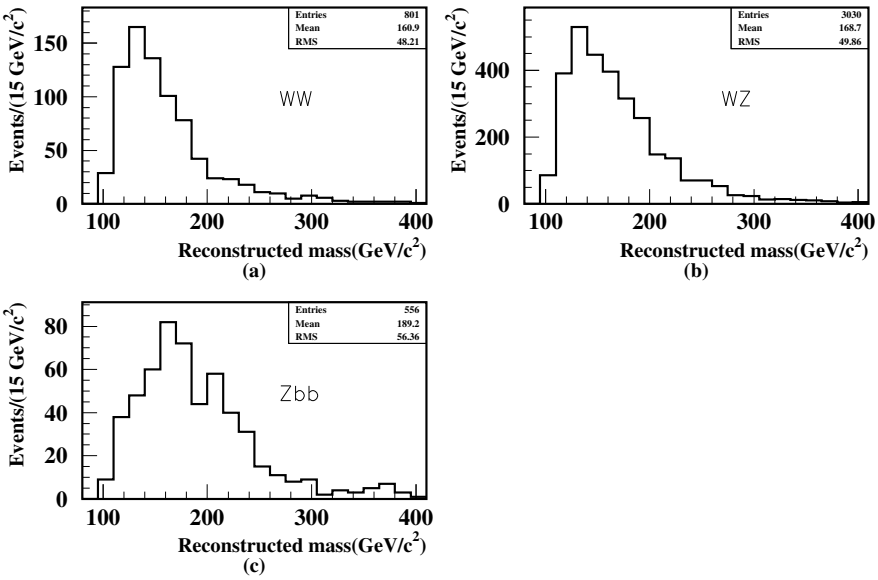

Figure 5.2: Reconstructed top mass distributions for PYTHIA WW (a), PYTHIA WZ (b), and VECBOS Zbb (c).

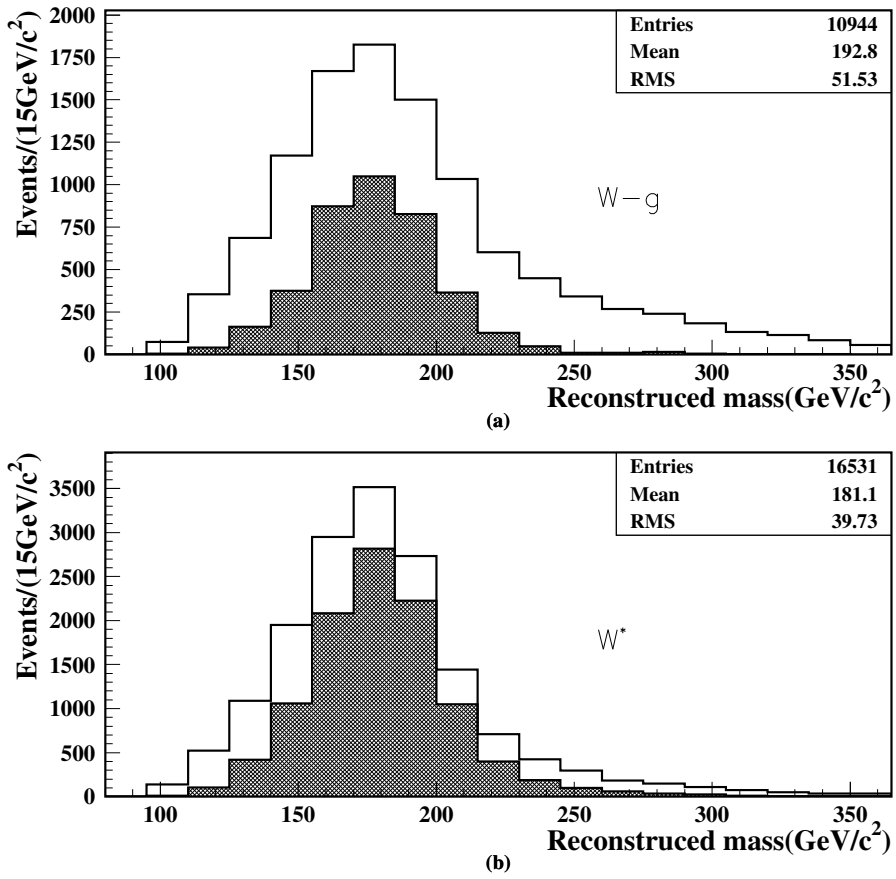

Figure 5.3: Reconstructed top mass distributions for single top through the W-gluon fusion process (a) and single top through the W^* process (b). Hatched histograms show the events with the right b-jet assignment.

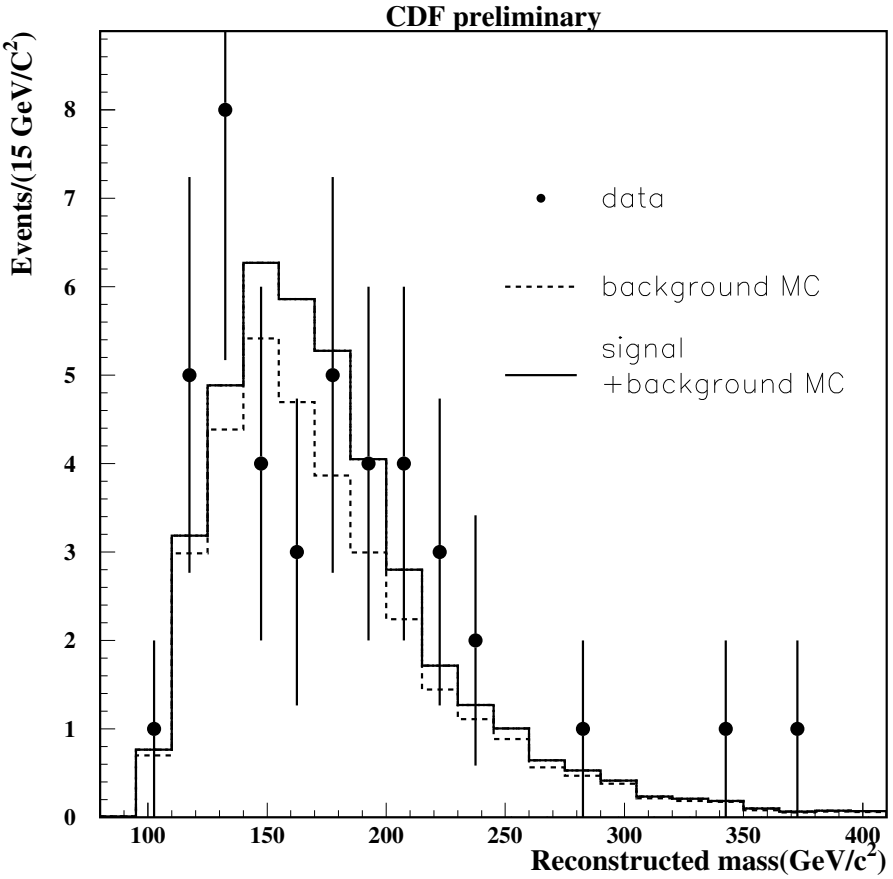

Figure 5.4: Reconstructed top mass distribution. The points show the data, the dashed histogram shows the fitted background, and the solid histogram shows fitted signal plus background.

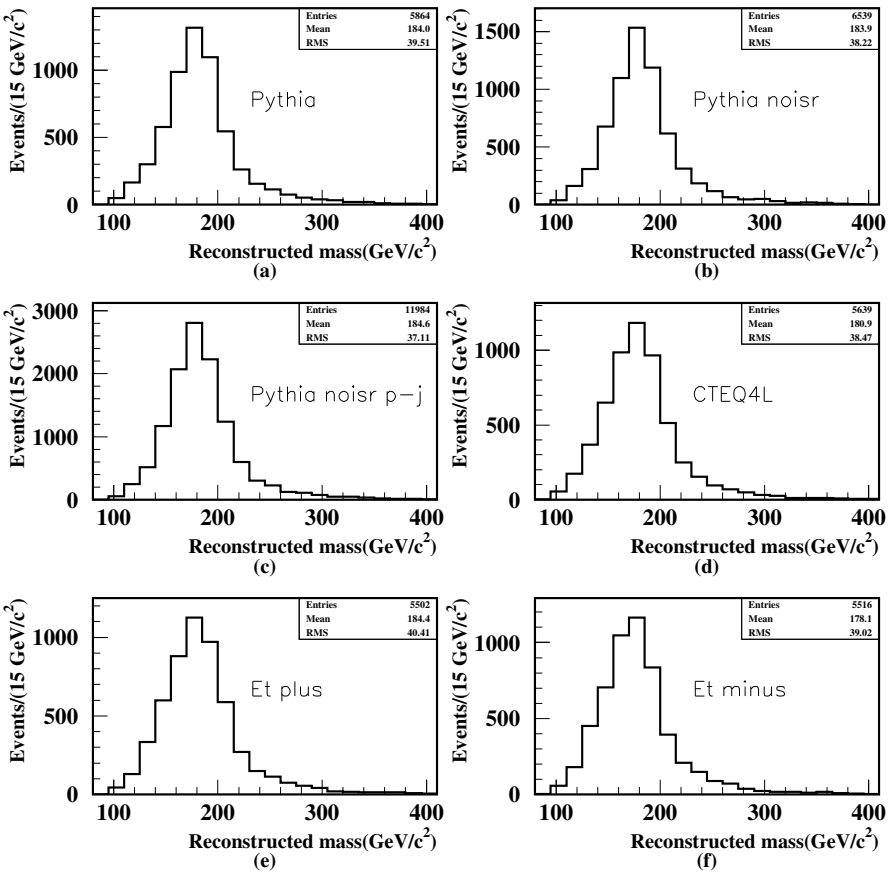

Figure 5.5: Reconstructed top mass distributions for s-channel W^* signal events generated with standard PYTHIA Monte Carlo (a), PYTHIA with no initial state radiation (b), with no initial state and with parton -jet matching (c), HERWIG with parton distribution of CTEQ4L (d), with positively shifted jet energy (e) and with negatively shifted jet energy (f).

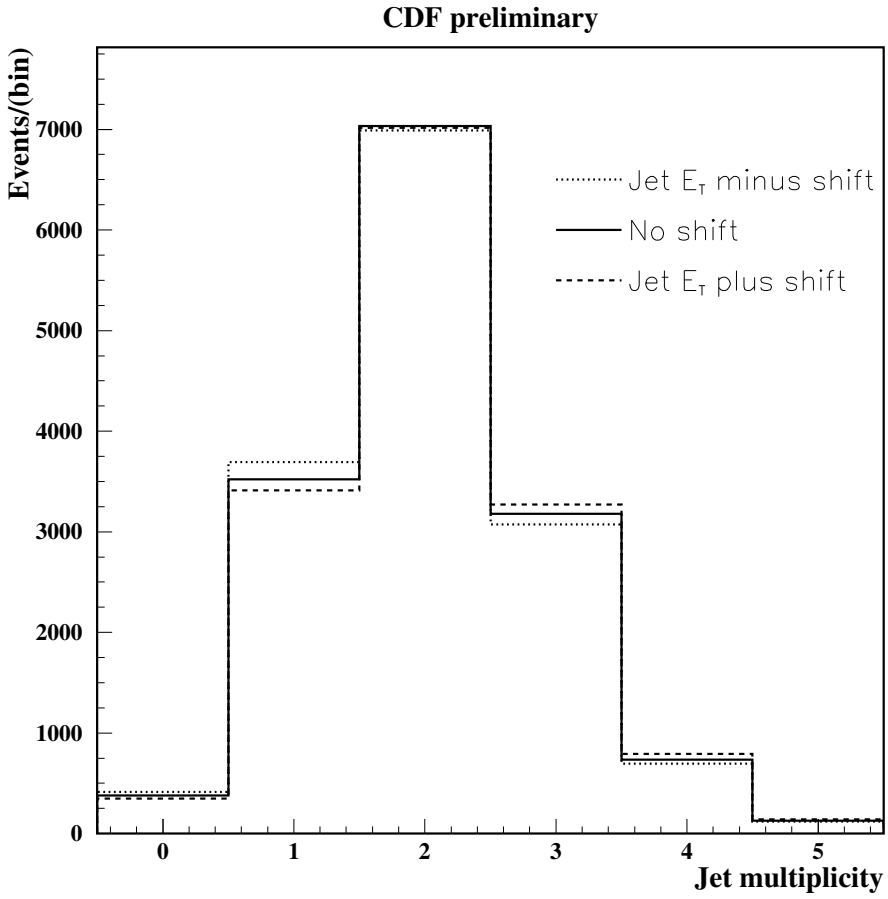

Figure 5.6: Jet multiplicity distribution with uncorrected $E_T > 15$ GeV and $|\eta| < 2.0$ for s-channel W^* signal Monte Carlo. The solid histogram is that for the default jet energy scale, the dotted histogram is for negatively shifted jet E_T, and the dashed histogram is for positively shifted jet E_T.

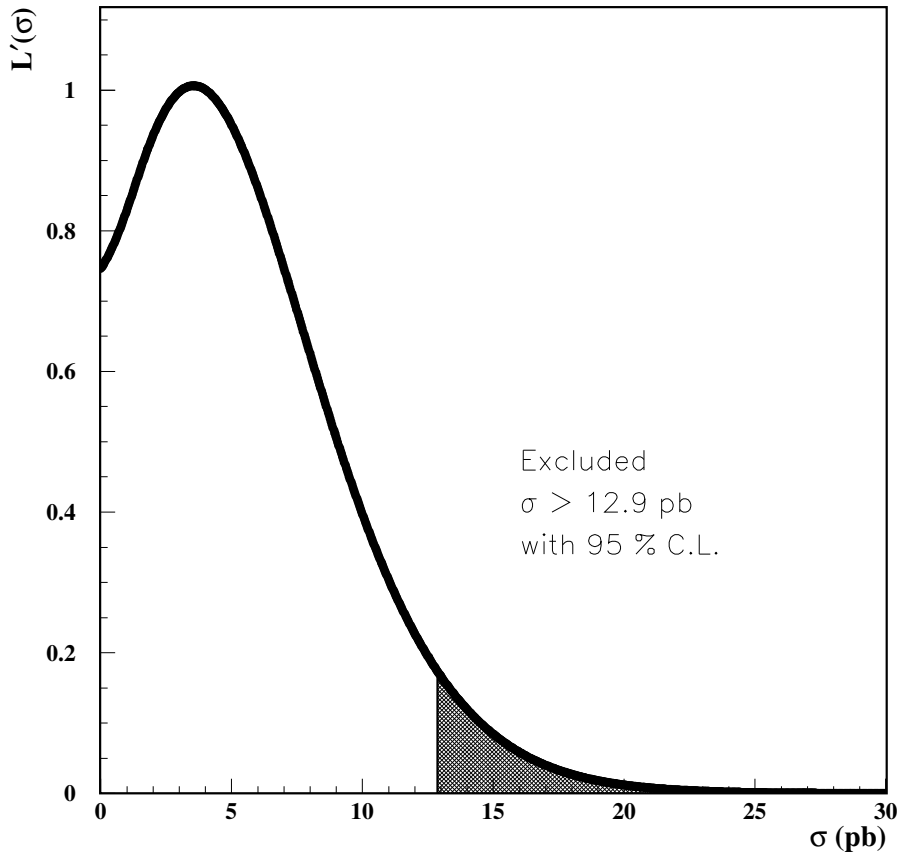

Figure 5.7: Smeared likelihood $L'(\sigma)$ as a function of the W^* single top cross section in the data.

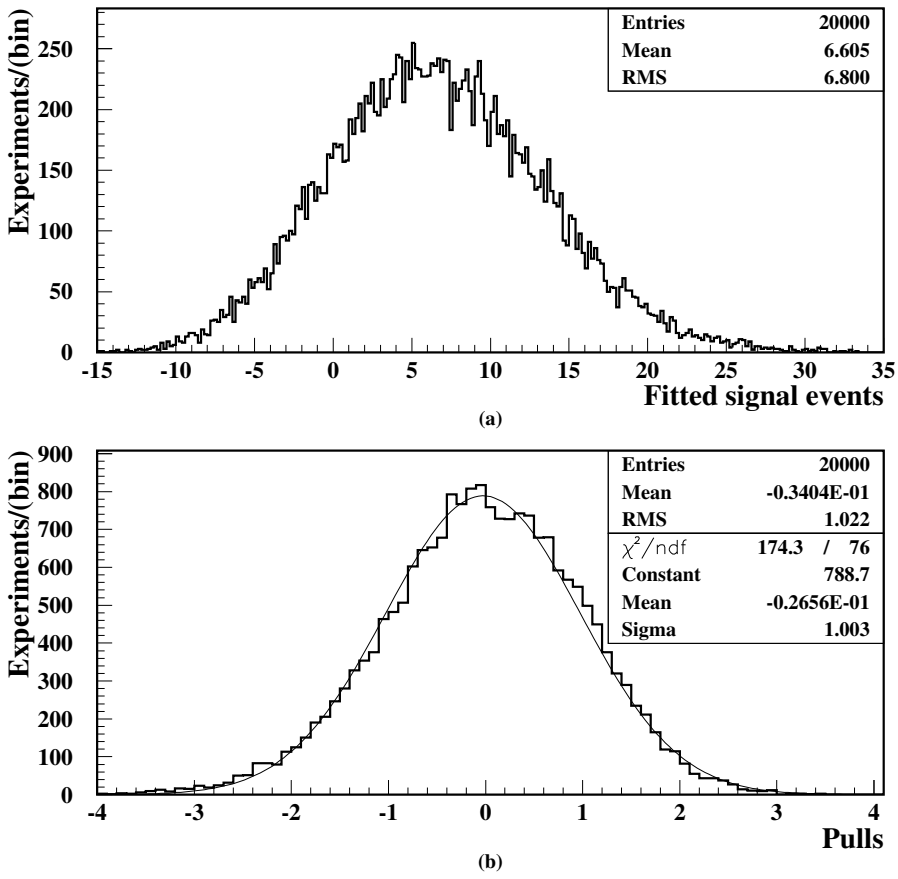

Figure 5.8: Test of the likelihood fit with pseudo-experiments consisting of N_b background and N_s signal events, where N_b is a Poisson fluctuation of the number of events predicted in Table 5.1, and N_s is a Poisson fluctuation of the fit result on the data (6.6 events). The distribution of the fitted number of signal events (a) and the corresponding pulls distribution (b).

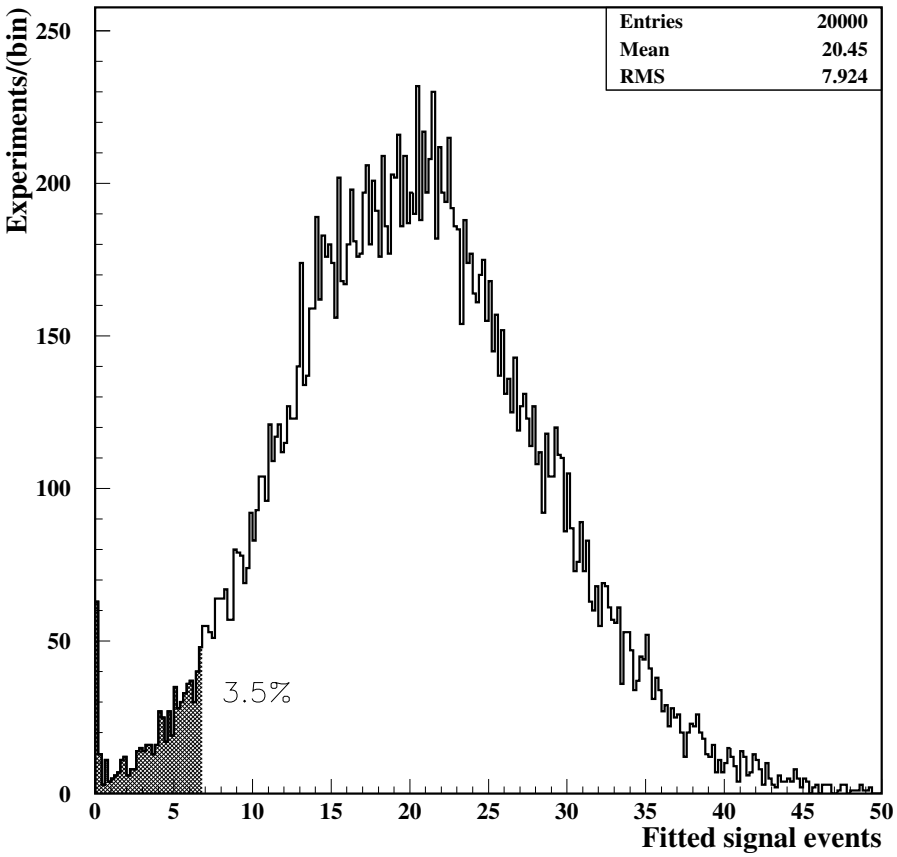

Figure 5.9: Distribution of the fitted number of signal events for pseudo-experiment samples. Each sample consists of N_b background and N_s signal events, where N_b is a Poisson fluctuation of the number of events predicted in Table 5.1, and N_s is a Poisson fluctuation of the unsmeared upper limit on the signal. The fitted number of signal events is equal to or less than 6.6 events in 3.5% of the pseudo-experiments.

Chapter 6

Upper limit on the combined cross section of single top quark production via the s-channel W^* and W-gluon fusion processes

In this section we extract an upper limit on the combined cross section of the single top quark production via the s-channel W^* and the W-gluon fusion processes. We perform the likelihood fit which is the combination of the likelihoods for the Q$\times\eta$ distribution used in Chapter 4 and for the reconstructed top mass distribution used in Chapter 5. We use only double b-tagged events for the fit of the reconstructed top mass distribution instead of at least one SVX b-tagged events. and use the remaining single b-tagged events for the Q$\times\eta$ distribution in order to

have two independent samples.

6.1 Likelihood fit

We define the likelihoods as follows:

$$L(\mu_{1t\bar{t}}, \mu_{1QCD}, \mu_{2t\bar{t}}, \mu_{2QCD}, \sigma_{Wg}, \sigma_{W^*}) = L_1(\mu_{1t\bar{t}}, \mu_{1QCD}, \sigma_{Wg}, \sigma_{W^*}) \times L_2(\mu_{2t\bar{t}}, \mu_{2QCD}, \sigma_{Wg}, \sigma_{W^*}) \quad (6.1)$$

$$L_1(\mu_{1t\bar{t}}, \mu_{1QCD}, \sigma_{Wg}, \sigma_{W^*}) = \frac{e^{-\frac{1}{2}\left(\frac{\mu_{1t\bar{t}} - n_{1t\bar{t}}}{\Delta_{1t\bar{t}}}\right)^2}}{\sqrt{2\pi}\Delta_{1t\bar{t}}} \times \frac{e^{-\frac{1}{2}\left(\frac{\mu_{1\mathrm{QCD}} - n_{1\mathrm{QCD}}}{\Delta_{1\mathrm{QCD}}}\right)^2}}{\sqrt{2\pi}\Delta_{1\mathrm{QCD}}} \times \prod_i \frac{e^{-\mu_{1i}} \cdot \mu_{1i}^{n_{1i}}}{n_{1i}!} \quad (6.2)$$

$$L_2(\mu_{2t\bar{t}}, \mu_{2QCD}, \sigma_{Wg}, \sigma_{W^*}) = \frac{e^{-\frac{1}{2}\left(\frac{\mu_{2t\bar{t}} - n_{2t\bar{t}}}{\Delta_{2t\bar{t}}}\right)^2}}{\sqrt{2\pi}\Delta_{2t\bar{t}}} \times \frac{e^{-\frac{1}{2}\left(\frac{\mu_{2\mathrm{QCD}} - n_{2\mathrm{QCD}}}{\Delta_{2\mathrm{QCD}}}\right)^2}}{\sqrt{2\pi}\Delta_{2\mathrm{QCD}}} \times \prod_i \frac{e^{-\mu_{2i}} \cdot \mu_{2i}^{n_{2i}}}{n_{2i}!} \quad (6.3)$$

where:

- L_1, L_2 = the likelihoods for the $Q \times \eta$ distribution and the reconstructed top mass distribution, respectively.
- $\mu_{1t\bar{t}}$, μ_{1QCD}, $\mu_{2t\bar{t}}$, μ_{2QCD} = fit parameters representing the numbers of $t\bar{t}$ and QCD events in the data. $\mu_{1t\bar{t}}$ and μ_{1QCD} are parameters for the fit of the $Q \times \eta$ distribution on the single b-tagged events. $\mu_{2t\bar{t}}$ and μ_{2QCD} are parameters for the fit of the reconstructed top mass distribution. The suffix 1 and 2 in the variables represent the numbers for the single b-tagged sample and the double b-tagged sample, respectively.

- n_{1QCD}, $n_{1t\bar{t}}$, n_{2QCD}, $n_{2t\bar{t}}$ = expected numbers of events from QCD and $t\bar{t}$. ($n_{1QCD} = 10.2$, $n_{1t\bar{t}} = 2.2$, $n_{2QCD} = 1.6$, $n_{2t\bar{t}} = 1.0$).

- Δ_{1QCD}, $\Delta_{1t\bar{t}}$ = uncertainties on the expected numbers of events from QCD and $t\bar{t}$. ($\Delta_{1QCD} = 2.0$, $\Delta_{1t\bar{t}} = 0.6$, $\Delta_{2QCD} = 0.4$, $\Delta_{2t\bar{t}} = 0.3$).

- $\mu_{1i} = \mu_{1QCD} \cdot \alpha_{1i} + \mu_{1t\bar{t}} \cdot \beta_{1i} + \sigma_{Wg} \cdot \mathcal{L} \cdot A_{1Wg} \cdot \gamma_{1i} + \sigma_{W^*} \cdot \mathcal{L} \cdot A_{1W^*} \cdot \delta_{1i}$, $\mu_{2i} = \mu_{2QCD} \cdot \alpha_{2i} + \mu_{2t\bar{t}} \cdot \beta_{2i} + \sigma_{Wg} \cdot \mathcal{L} \cdot A_{2Wg} \cdot \gamma_{2i} + \sigma_{W^*} \cdot \mathcal{L} \cdot A_{2W^*} \cdot \delta_{2i}$, where α_{ji}, β_{ji}, γ_{ji} and δ_{ji} (j=1 or 2) are the expected fractions of QCD, $t\bar{t}$, Wg and W^* events that enter the i-th bin. $\mathcal{L}$ is the integrated luminosity. A_{1Wg}, A_{1W^*}, A_{2Wg}, A_{2W^*} are the acceptances for the signals.

- n_{1i}, n_{2i} = observed number of events in the i-th bin of the Q$\times\eta$ distribution and the reconstructed top mass distribution.

We use the Q$\times\eta$ distributions shown in Figures 4.6 and the reconstructed top mass distributions shown in Figures 6.1. We have an independent free parameter for each signal process, W-gluon fusion process and s-channel W^* process, in this search. We use a $Wb\bar{b}$ Monte Carlo sample to model the QCD background. This sample includes 12,893 single b-tagged events and 4,169 double b-tagged events. The fit results are listed in Table 6.1. The fitted Q$\times\eta$ distribution and reconstructed top mass distribution are shown in Figure 6.2 and Figure 6.3. We extract the fitted combined cross section $\sigma_{Wg} + \sigma_{W^*}$ from the point (σ_{Wg} ,σ_{W^*}) = (3.0 pb, 7.2 pb) and (0.0 pb, 1.9 pb), which are the a maximum and minimum points of $\sigma_{Wg} + \sigma_{W^*}$, respectively, in the region

$-log(L) < -log(L_{minimum}) + 0.5$. The extracted combined cross section is $5.2^{+4.9}_{-3.4}$ pb.

	input	output
μ_{1QCD}	10.2 ± 2.0	10.0 ± 1.9
$\mu_{1t\bar{t}}$	2.2 ± 0.6	2.2 ± 0.6
μ_{2QCD}	1.6 ± 0.4	1.6 ± 0.4
$\mu_{2t\bar{t}}$	1.0 ± 0.3	0.9 ± 0.2
σ_{Wg}	free	$0.0\ ^{+4.8}_{-0.0}$
σ_{W^*}	free	$5.2\ ^{+4.0}_{-3.4}$

Table 6.1: Fit parameter input and output values for the binned likelihood fit.

6.2 Cross section limit

We extract a 95 % C.L. upper limit on the combined cross section σ_{95} which is given by:

$$\int\int_{\sigma_{Wg}+\sigma_{W^*}<\sigma_{95}} L(\sigma_{Wg},\sigma_{W^*})d\sigma_{Wg}d\sigma_{W^*} = 0.95 \times \int_0^\infty \int_0^\infty L(\sigma_{Wg},\sigma_{W^*})d\sigma_{Wg}d\sigma_{W^*},$$

The integral region of the left side of the equation lies below the line $\sigma_{Wg} + \sigma_{W^*} = \sigma_{95}$. Figure 6.4 shows the likelihood $L(\sigma_{Wg},\sigma_{W^*})$. We extract the 95 % C.L. upper limit on the combined cross section of 17.1 pb.

6.3 Systematic uncertainty

6.3.1 The shapes of $Q \times \eta$ distribution and top mass distribution

For each source of systematic uncertainty we simulate the single top signal events and background events with the corresponding parameter shifted by one standard deviation (or some reasonable estimate thereof). For each pseudo-experiment, the number of background events is a Poisson fluctuation of the expected number. The number of signal events is fixed to 0 or a Poisson fluctuation of the 95% C.L. upper limit (= 17.1 pb). Q×η of each event is generated according to the Q×η distribution for the standard signal and background which are called standard templates. Then, we fit the Q×η distribution in a pseudo-experiment with a sum of standard signal and background templates and extract 95% C.L. upper limit on the combined cross section. We perform 200 pseudo-experiments and extract the median of the upper limits with the standard templates (σ_{95}). Next by fitting the above pseudo-experiment Q×η distribution with the shifted template, we extract the median of the upper limits with the shifted templates (σ'_{95}). The systematic uncertainty is extracted from the difference between them:

$$\frac{(\sigma'_{95} - \sigma_{95})}{\sigma_{95}}$$

We consider the following systematic uncertainties on the shape:

- Monte Carlo generator

We take the difference between HERWIG and PYTHIA as systematic uncertainty. The estimated uncertainty on the cross section limit is +0.7% for input signal $\sigma_{singletop} = 0$ pb and +1.0% for $\sigma_{singletop} = 95\%$ C.L. upper limit.

- Initial state radiation (ISR)

  We take a half the difference between PYTHIA without initial state radiation and standard PYTHIA. The corresponding systematic uncertainty on the cross section limit is −0.4% for input signal $\sigma_{singletop} = 0$ pb and −0.8% for $\sigma_{singletop} = 95\%$ C.L. upper limit.

- Final state radiation (FSR)

  We take a half the difference between PYTHIA-noISR and PYTHIA-noISR where the two jets match the GENP-level partons within a cone of 0.4. The corresponding systematic uncertainty on the cross section limit is −0.2% for input signal $\sigma_{singletop} = 0$ pb and −0.2% for $\sigma_{singletop} = 95\%$ C.L. upper limit.

- Parton distribution functions (PDF)

  We symmetrize the difference between CTEQ4L and MRSD_' (our standard choice of PDF is the latter). The corresponding systematic uncertainty on the cross section limit is −0.7% for input signal $\sigma_{singletop} = 0$ pb and −1.2% for $\sigma_{singletop} = 95\%$ C.L. upper limit.

- Jet energy scale

  We shift the energy by hand in the same way as Section 5.4.1. We take the average of the difference between the positive shift and the standard and the difference between the negative shift and the

standard. The corresponding systematic uncertainty on the cross section limit is 0.4% for input signal $\sigma_{singletop} = 0$ pb and 0.4% for $\sigma_{singletop} = 95\%$ C.L. upper limit.

- Background modelling

  Our standard QCD background model is VECBOS $Wb\bar{b}$. As an alternate model we combine PYTHIA Wc and VECBOS $Wb\bar{b}$ with a ratio of Wc:Wbb=3:7. We take the difference between the standard background and the alternate background. The corresponding systematic uncertainty on the cross section limit is -0.4% for input signal $\sigma_{singletop} = 0$ pb and -0.2% for $\sigma_{singletop} = 95\%$ C.L. upper limit.

Table 6.2 lists the systematic uncertainties on the shape.

Systematic	The shift on the cross section upper limit		The uncertainty on the cross section upper limit
	$\sigma_{singletop} = 0$ pb	$\sigma_{singletop} = 95\%$ upper limit	
Parton distributions	-0.7 %	-1.2 %	1.2 %
Signal generator	$+0.7$ %	$+1.0$ %	1.0 %
Initial state radiation	-0.4 %	-0.8 %	0.8 %
Jet energy scale	0.4 %	0.4 %	0.4 %
Background	-0.4 %	-0.2 %	0.4 %
Final state radiation	-0.2 %	-0.2 %	0.2 %

Table 6.2: Shift on the cross section limit due to the shape uncertainty

6.3.2 The acceptance of event selection

To estimate the systematic uncertainty on the cross section limit due to the acceptance, we modify the likelihood from L to L':

$$L' = \frac{e^{-\frac{1}{2}\left(\Delta_{\mu_{\rm acc}}\right)^2}}{\sqrt{2\pi}} \times L_1 \times L_2$$

where, $\Delta_{\mu_{acc}}$ is a fit parameter representing the acceptance uncertainty relative to the acceptance. μ_i in the equations (6.2) and (6.3) is changed to

$$\mu_i = \mu_{QCD}\cdot\alpha_i + \mu_{t\bar{t}}\cdot\beta_i + (1+\Delta_{\mu_{acc}}\cdot\Delta_{Wg})\cdot\mu_{Wg}\cdot\gamma_i + (1+\Delta_{\mu_{acc}}\cdot\Delta_{W^*})\cdot\mu_{W^*}\cdot\delta_i$$

,

where Δ_{Wg} and Δ_{W^*} are the uncertainty on the acceptance for W-gluon fusion and W^* single top, respectively. Δ_{Wg} and Δ_{W^*} are given for single b-tagged events and for double b-tagged events separately. The acceptance systematic uncertainty is extracted from the difference between the medians of the upper limits with the standard likelihood function L and the modified likelihood function L' in the same way as the shape systematic uncertainty.

- Monte Carlo generator

  We take the difference between HERWIG and PYTHIA. Δ_{Wg} and Δ_{W^*} are -9% and 4% for the likelihood L_1, respectively, and 141% and 11% for the likelihood L_2. The uncertainty of 141% is extracted from the difference between the HERWIG expectation of 0.038 events and the PYTHIA expectation of 0.084 events. The

uncertainty on the cross section limit is +0.8% for input signal $\sigma_{singletop} = 0$ pb and +0.9% for $\sigma_{singletop} = 95\%$ C.L. upper limit.

- Initial state radiation (ISR)

  We take a half the difference between PYTHIA without initial state radiation and standard PYTHIA as the input. Δ_{Wg} and Δ_{W^*} are 7% and 6% for the L_1, respectively, and -45% and 7% for the L_2. The estimated uncertainty on the cross section limit is +0.5% for input signal $\sigma_{singletop} = 0$ pb and +0.6% for $\sigma_{singletop} = 95\%$ C.L. upper limit.

- Final state radiation (FSR)

  We take a half the difference between PYTHIA-noISR and PYTHIA-noISR where the two jets match the GENP-level partons within a cone of 0.4. Δ_{Wg} and Δ_{W^*} are -7% and -6% for the L_1, respectively, and -4% and -1% for the L_2. The estimated uncertainty on the cross section limit is -0.0% for input signal $\sigma_{singletop} = 0$ pb and -0.1% for $\sigma_{singletop} = 95\%$ C.L. upper limit.

- Parton distribution functions (PDF)

  We symmetrize the difference between CTEQ4L and MRSD_' (our standard choice of PDF is the latter). Δ_{Wg} and Δ_{W^*} are -1% and -1% for the L_1, respectively, and -13% and 5% for the L_2. The estimated uncertainty on the cross section limit is 0.0% for input signal $\sigma_{singletop} = 0$ pb and -0.3% for $\sigma_{singletop} = 95\%$ C.L. upper limit.

- Jet energy scale

We shifted the energy by hand in the same way as Section 5.4.1. We take the average of the difference between positive shift and standard and the difference between negative shift and standard. Δ_{Wg} and Δ_{W^*} are 1% for both single b-tagged and double b-tagged events. The estimated uncertainty on the cross section limit is 0.0% for input signal $\sigma_{singletop} = 0$ pb and 0.1% for $\sigma_{singletop} = 95\%$ C.L. upper limit.

- Trigger and Lepton ID

  Δ_{Wg} and Δ_{W^*} are 10% for both single b-tagged and double b-tagged events in the same way as Section 4.3.2. The estimated uncertainty on the cross section limit is +5.0% for input signal $\sigma_{singletop} = 0$ pb and +5.8% for $\sigma_{singletop} = 95\%$ C.L. upper limit.

- B-tagging

  The uncertainty due to b-tagging comes from the uncertainty of the scale factor 1.0 $\pm$ 0.1 for SECVTX b-tagging and 0.95 $\pm$ 0.14 for SLT b-tagging. Δ_{Wg} and Δ_{W^*} are 10% for single b-tagged events and 11% for double b-tagged events. The estimated uncertainty on the cross section limit is +5.2% for input signal $\sigma_{singletop} = 0$ pb and +6.1% for $\sigma_{singletop} = 95\%$ C.L. upper limit.

- Luminosity

  The uncertainty due to luminosity is 4% from 106.0 $\pm$ 4.1 pb^{-1}. Δ_{Wg} and Δ_{W^*} are 4% for both single b-tagged and double b-tagged events. The estimated uncertainty on the cross section limit is +0.8% for input signal $\sigma_{singletop} = 0$ pb and +0.7% for $\sigma_{singletop} =$

95% C.L. upper limit.

Tables 6.3 and 6.4 list the Δ_{Wg} and Δ_{W^*} in the likelihood L_1 and in the likelihood L_2, respectively. Table 6.5 lists the systematic uncertainties on the acceptance for both single b-tagged events and double b-tagged events.

Since the uncertainties on the shape and acceptance from the same systematic source correlate with each other by 100 %, we add the two systematic uncertainties in the same source. Then we add all systematic uncertainties in a quadrature. The total systematic uncertainty is 8.9% as listed in Table 6.6. Next we obtain the systematic uncertainty on the fitted cross section. The systematic uncertainty due to the acceptance uncertainty is extracted from the shift of the peak position of the likelihood $L(\sigma_{Wg}, \sigma_{W^*})$ extracted with the data by shifting the acceptance uncertainty on each single top process listed in Table 6.3 and 6.4. The uncertainty due to the shape is extracted in the same way as the upper limit. The total systematic uncertainty on the fitted cross section is 27%. It results in $\sigma_{Wg+W^*} = 5.2^{+4.9}_{-3.4}$ (stat) $\pm$ 1.4(syst) pb. The 95 % C.L. upper limit on the combined cross section with systematic uncertainty is defined to be the one shifted positively by one standard deviation from the limit without systematic uncertainty. We extract it to be 18.6 pb.

Systematic	Relative uncertainty	
	Δ_{Wg}	Δ_{W^*}
Trigger+lepton ID	10 %	10 %
Signal generator	−9 %	4 %
B-tagging	10 %	10 %
Initial state radiation	7 %	6 %
Final state radiation	−7 %	−6 %
Luminosity	4 %	4 %
Parton distributions	−1 %	−1 %
Jet energy scale	1 %	1 %

Table 6.3: Input of the uncertainty affecting the acceptance in the likelihood L_1 for the single b-tagged events.

Systematic	Relative uncertainty	
	Δ_{Wg}	Δ_{W^*}
Trigger+lepton ID	10 %	10 %
Signal generator	141 %	11 %
B-tagging	11 %	11 %
Initial state radiation	−45 %	7 %
Final state radiation	−4 %	−1 %
Luminosity	4 %	4 %
Parton distributions	−13 %	5 %
Jet energy scale	1 %	1 %

Table 6.4: Input of the uncertainty affecting the acceptance in the likelihood L_2 for the double b-tagged events.

Systematic	The shift on the cross section upper limit		The uncertainty on the cross section upper limit
	$\sigma_{singletop} = 0$ pb	$\sigma_{singletop} = 95\%$ upper limit	
Trigger+lepton ID	+5.0 %	+5.8 %	5.8 %
B-tagging	+5.2 %	+6.1 %	6.1 %
Signal generator	+0.8 %	+0.9 %	0.9 %
Initial state radiation	+0.5 %	+0.6 %	0.6 %
Luminosity	+0.8 %	+0.7 %	0.8 %
Final state radiation	-0.0 %	-0.1 %	0.1 %
Parton distributions	0.0 %	-0.3 %	0.3 %
Jet energy scale	0.0 %	0.1 %	0.1 %

Table 6.5: Shift on the cross section limit due to the acceptance

Systematic	shape	acceptance	shape+acc.
Trigger+lepton ID	-	5.8 %	5.8 %
B-tagging	-	6.1 %	6.1 %
Signal generator	1.0 %	0.9 %	1.9 %
Initial state radiation	0.8 %	0.6 %	1.4 %
Background	0.4 %	-	0.4 %
Luminosity	-	0.8 %	0.8 %
Final state radiation	0.2 %	0.1 %	0.3 %
Parton distributions	1.2 %	0.3 %	1.5 %
Jet energy scale	0.4 %	0.0 %	0.4 %
Total			8.9 %

Table 6.6: Shift on the cross section

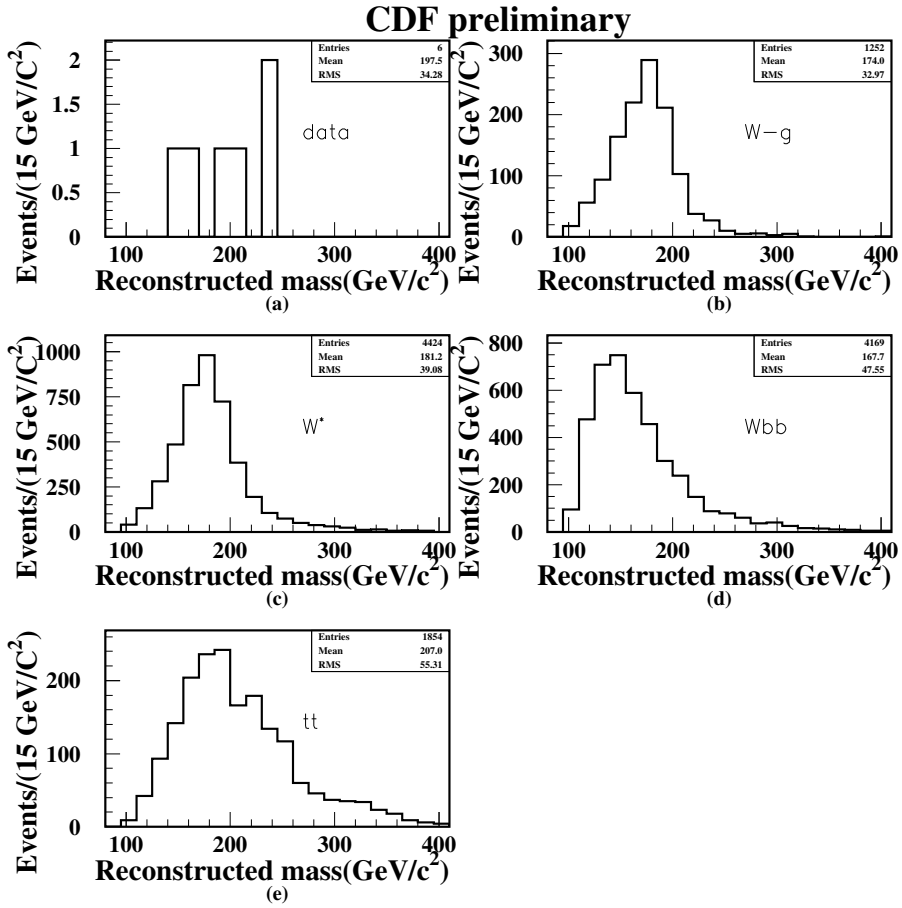

Figure 6.1: Reconstructed top mass distributions for data (a), single top in the W-gluon fusion channel (b), single top in the $W^\star$ channel (c), VECBOS $Wb\bar{b}$ (d), and HERWIG $t\bar{t}$ (e), after selection of double b-tagged events.

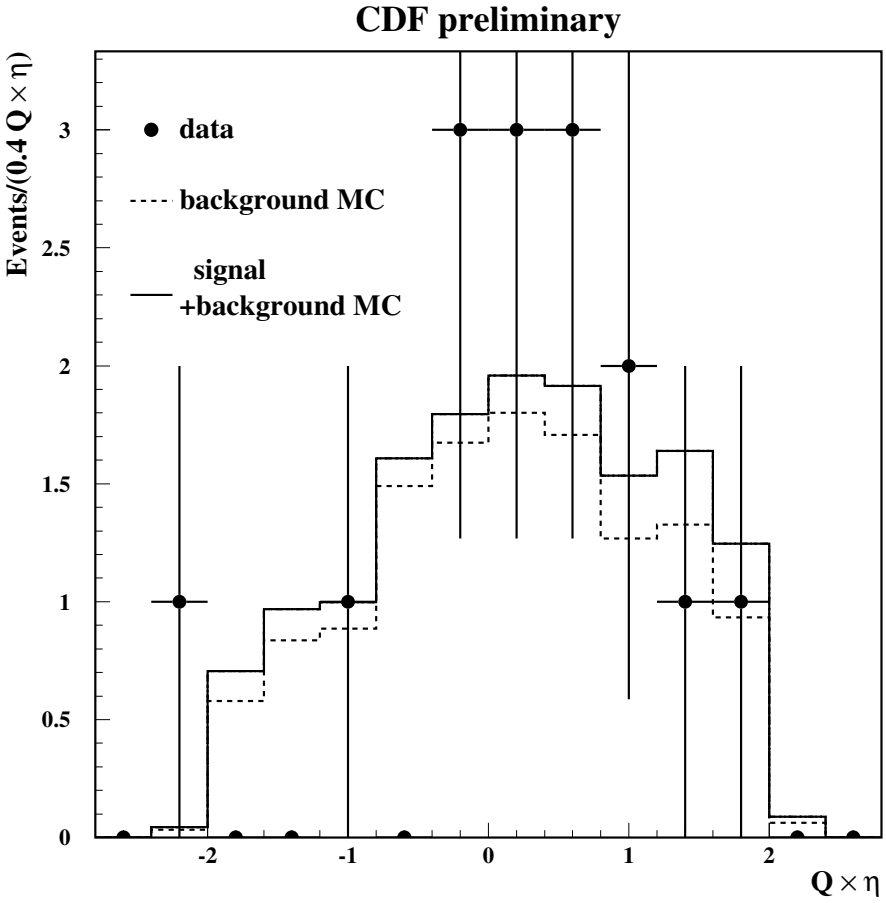

Figure 6.2: Fitted Q×η distribution. The points show the data, the dashed histogram shows the fitted background, and the solid histogram shows the fitted signal plus background.

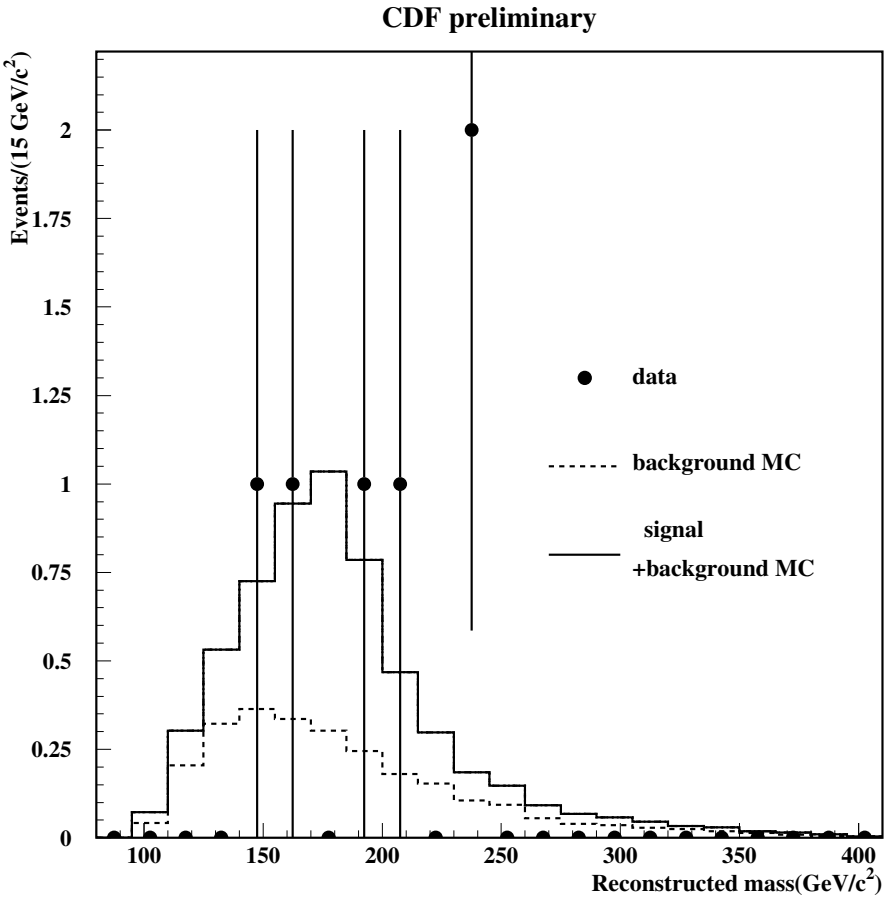

Figure 6.3: Fitted reconstructed top mass distribution for double b-tagged W+2 jet events. The points show the data, the dashed histogram shows the fitted background, and the solid histogram shows fitted signal plus background.

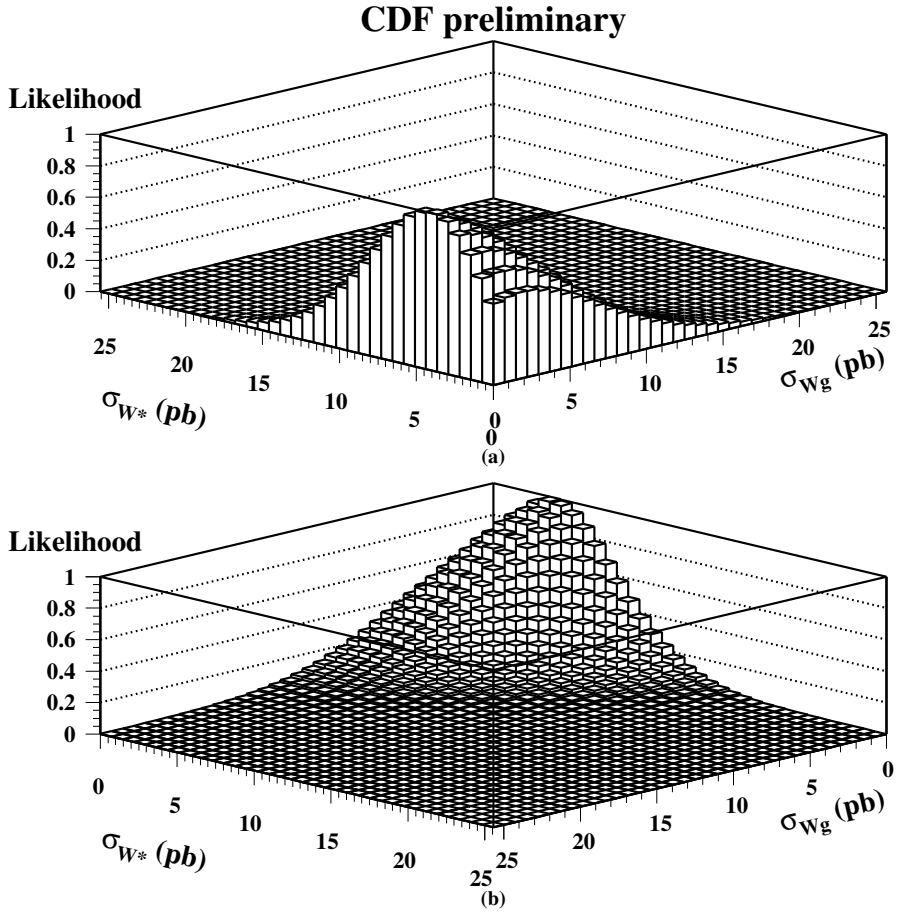

Figure 6.4: The likelihood $L(\sigma_{Wg}, \sigma_{W^*})$

Chapter 7

Conclusion

We searched for the single top quark production through the W-gluon fusion process and the s-channel W^* process in proton-antiproton collisions at $\sqrt{s} = 1.8$ TeV with an integrated luminosity of 106 $\pm$ 4.1 pb^{-1}.

We select b-tagged W + 2 jet events by requiring a high P_T isolated electron or muon and a high $\not\!\!E_T$ and two jets, at least one of which is identified as a b-quark jet. We observe 42 b-tagged W + 2 jet events while we expect a total background of 29.7 ± 4.7 events, 1.8 ± 0.3 signal events in W-gluon fusion process and 1.2 ± 0.2 signal events in s-channel W^* process.

For the search for single top quark production through W-gluon fusion process, we require the reconstructed top mass to be between 145 and 205 GeV/c^2 and remove the double b-tagged events for the above b-tagged W + 2 jet sample and observe fifteen events while we expect a total background of 13.1 ± 2.1 events and 1.4 ± 0.3 signal events. The likelihood fit of the $Q \times \eta$ distribution for this sample yields $1.3^{+4.2}_{-1.3}$ signal events.

The upper limit on the cross section of the single top production in this channel at the 95 % confidence level is found to be 13.5 pb. For the search for single top quark production through the s-channel W^* process, we use the b-tagged W+2 jet events and perform a likelihood fit of the reconstructed top mass distribution. From the fit, we extract $6.4^{+7.3}_{-6.4}$ signal events and an upper limit of 12.9 pb on the production cross section at 95% confidence level.

We also obtain an upper limit on the combined cross section of single top quark production via the s-channel W^* and W-gluon fusion processes. We measure a combined cross section of single top production to be $5.2^{+4.9}_{-3.4}$(stat)$\pm$1.4(syst) pb and extract an upper limit of 18.6 pb on the single top production cross section at 95% confidence level.

Bibliography

[1] F.Abe *et. al* Phys. Rev. D 50 2966 (1994).

[2] F.Abe *et. al* Phys .Rev. Lett. **74** 2626(1995).

[3] S.Abachi *et. al* Phys .Rev. Lett. **74** 2632(1995).

[4] The top averaging group, FERMILAB-TM-2084.

[5] Particle Data Group, European Physical Journal C, Vol 3, 343 (1998).

[6] T.Stelzer, Z.Sullivan, S.Willenbrock, Phys. Rev. D **58**, 094021 (1998).

[7] M.C.Smith, S.Willenbrock, Phys. Rev. D **54**, 6696 (1996).

[8] T.Tait, C.P.Yuan, hep-ph/9710372.

[9] A.Heinson, A.Beyaev and E.Boos Phys .Rev. D **56** 3114 (1997).

[10] F.Abe *et. al* Nucl. Instr. and Meth. A271 387 (1988).

[11] F.Abe *et. al* Phys. Rev. Lett. 80 2773 (1998).

[12] H. Minemura *et. al* Nucl. Instr. and Meth. A238 18 (1985).

[13] D.Amidei *et. al* Nucl. Instr. and Meth. A350 73 (1994).

[14] D.Amidei *et. al* Nucl. Instr. and Meth. A342 251 (1994).

[15] C.Haber *et. al* Nucl. Instr. and Meth. A289 388 (1990).

[16] M.Kruse Ph.D thesis Purdue university (1996).

[17] F.Abe *et. al* Phys. Rev. D 45 1448 (1992);

[18] F.Abe *et. al* Phys. Rev. D 47 4857 (1993).

[19] F.Abe *et. al* Phys. Rev. Lett. 79 3819 (1997).

[20] G.Marchesini and B.R Webber Nucl. Phys. B301, 461 (1988);

[21] G.Marchesini *et. al* Comut. Phys. Comm. 67 405 (1992).

[22] T.Sjostarad, Comput. Phys. Comm. 39 347 (1986);

[23] T.Sjostarad and M.Bengtsson Comput. Phys. Comm. 46 43 (1987).

[24] P.Avery, K.Read, G.Trahern, Cornell Internal Note CSN-212, March 25, 1985 (unpublished).

[25] F.A.Berends, W.T.Giele, H.Kuijf and B.Tansk, Nucl. Phys. B357, 32 (1991).

[26] J. Ohnemus, Phys. Rev. D **44**, 1403 (1991);

[27] J. Ohnemus, Phys. Rev. D **44**, 3477 (1991).

[28] The top group, CDF internal note 5043.

[29] C.P.Yuan, Phys. Rev. D **41**, 42 (1990).

[30] A.D. Martin, R.G. Roberts and W.J.Stirling, Phys. Lett. **B306** 145 (1993).

[31] H.L.Lai *et. al.*, Phys Rev. D **55**, 1280 (1997).

[32] F.Abe *et al.* (CDF Collaboration), Phys. Rev. D **43**, 664 (1991).

[33] S.Cortese and R.Petronzio, Phys. Lett. B **253**, 494 (1991).

[34] F.Abe *et. al* Phys .Rev. Lett. **80** 2767(1998).

[35] CDF internal note 3983.